1238

APPLIED SCIENCE ASSOCIATES, INC.

105 EAST CHATHAM STREET
APEX, NORTH CAROLINA 27502
PHONE (919) 362-9311

STUDIES RELATED TO OCEAN DYNAMICS

Final Report for Task 3.2:

Aircraft Field Test Program To Investigate The Ability Of Remote Sensing Methods To Measure Current/Wind-Wave Interactions

by

N. E. Huang
W. A. Flood
G. S. Brown

May, 1975

Prepared under

NASA Contract No. NAS6-2520

for

National Aeronautics and Space Administration

Wallops Flight Center

Wallops Island, Virginia 23337

TABLE OF CONTENTS

LIST OF FIGURES

LIST OF FIGURES (Cont'd.)

INTRODUCTION

This report consists of two parts. Part I provides the theory and results of an experimental program to test the feasibility of remote sensing of current flows in the ocean and was written by Norden Huang. Part II is a summary of an analytical study of the feasibility of remote sensing of ocean currents by means of backscattering cross-section techniques and was written by W. A. Flood and G. S. Brown.

The experimental results in Part I represent the contributions of many investigators. Data analysis of the laser profilometer was provided by E. A. Uliana of Naval Research Laboratory; the probability density curves are the result of C. C. Tung of North Carolina State University; the data acquisition was supervised by Richard Shiel of Naval Research Laboratory and A. Gene Smith of Applied Science Associates, Inc.; and finally the ground truth data was provided by Marty Welch of North Carolina State University.

Part I - Theoretical and Experimental Results of the Remote Sensing of Ocean Currents.

1.0 INTRODUCTION

When waves propagate over the surface of the ocean their characteristics are modified continuously. The changes are drastic when they encounter a non-uniform current field. From a basic fluid mechanics point of view, this phenomenon has been studied by a number of investigators, such as: Longuet-Higgins and Stewart (1960, 1961, 1964), Crapper (1972). The application of the results as a means to measure the strength of the current has only been discussed recently (Huang, et al, 1972).

Through preliminary studies in the laboratory (Huang, et al, 1974), it was established that, for capillary waves, small scale currents could be accurately measured through observations of wave kinematics. The changes in gravity waves due to currents, however, have not yet been observed under controlled measurement conditions. From theoretical results and from casual observations of waves under natural conditions, drastic modifications of waves by changing currents have been noted and have provided ample justification to expect that whatever happened to capillary waves would also happen to gravity waves. However, because of practical limitations in the measurement technique used, the method employed for the capillary wave studies reported previously (Huang, et al, 1974) can not be used here. New methods and new theoretical groundwork will have to be developed. The theoretical developments required will be discussed in Chapter 2.

A field test at Hatteras Inlet, N. C., was conducted during the study. The test site was not chosen by scientific consideration; rather, the availability of ground truth data dictated the decision. The results of these tests showed qualitative support for the theoretical results. These will be discussed in Chapter 3. There were, however, problems in the data processing procedures and measurement techniques used. Recommendations for future improvements to aid in resolving these problems are given in the last chapter.

2.0 THEORETICAL STUDIES

2.1 Introduction

Interactions between currents and waves have been discussed by numerous authors, but in most of these studies, the directional properties of the wavefield have not been duly considered. As a result, unidirectional wave and current fields were assumed. Such approximation will probably hold in the open ocean where the horizontal scale of currents and wave fields are much longer than any single wave length; therefore, the wave field is approximately uniform in the horizontal variable both in amplitude and direction. Wave conditions at inlets, however, pose a different problem. The current field here is well defined and concentrated. The horizontal gradient of change is strong. Even if we neglect the influence of the bottom, the waves will still change direction as they propagate. This problem has been studied by Boone (1974) where directional and amplitude changes were investigated. A brief summary of Boone's results will be given first in the following discussion. The changes in wave characteristics will be discussed through the associated probability distribution functions.

2.2 Summary of the Equations for Inlet Wave Patterns

In developing the wave-current interaction equations in this study, the following assumptions are made:

(1) the tidal currents are assumed to be steady in time but non-uniform in space. This assumption holds because the periods of the wind waves and even the swells are of the order of seconds while the tidal period is of the order of hours. During the time a wave propagates through the tidal inlet, the current condition indeed will not change substantially, but the wave will experience completely different current conditions across the inlet;

(2) the motions of the fluid are assumed to be irrotational. This is more out of convenience of analysis than reality, but the assumption is good in most wave studies because the rotational influence is small in any case;

(3) the waves are assumed to be in deep water. There are some

difficulties with the deepwater assumption which requires that the depth of the water, D, be greater than one-half wave length, L/2; i.e. D/L > 1/2. The maximum depth at a typical inlet on the Outer Banks of North Carolina is of the order of 20 feet. Certainly any wave that has a length less than 40 feet will satisfy the deepwater criteria. However, the restriction is not critical for most cases in which we are interested. A wave of 100 feet in length, for example, will introduce an error of only 10%. This is well within the acceptable accuracy limit of the present capability in measurement techniques. In the future, a more precise model should be built for the shallow water case as well.

To begin the study of wave patterns, the kinematics involved will be considered. For the inlet geometry shown in Figure 2.1, under steady state conditions, by the kinematic conservation law discussed by Phillips (1966) we will have

$$\nabla n = 0 \tag{2.1}$$

where n represents the total frequency actually observed, which includes the pure oscillatory and convective frequencies, namely:

$$n = \underset{\sim}{k} \cdot (\underset{\sim}{U}+\underset{\sim}{c}) = \underset{\sim}{k}\cdot\underset{\sim}{U} + \sigma \tag{2.2}$$

In component form, equations 2.1 and 2.2 give:

$$k(U\cos\theta+c) = k_o c_o \tag{2.3}$$

where k is the wave number, U the current magnitude, c the phase speed, and θ the angle between the wave vector and the current direction. The subscript o indicates the condition when the current is zero.

For the deepwater gravity waves, the phase velocity and the wave number are related by

$$\frac{c^2}{c_o^2} = \frac{k_o}{k} \quad , \tag{2.4}$$

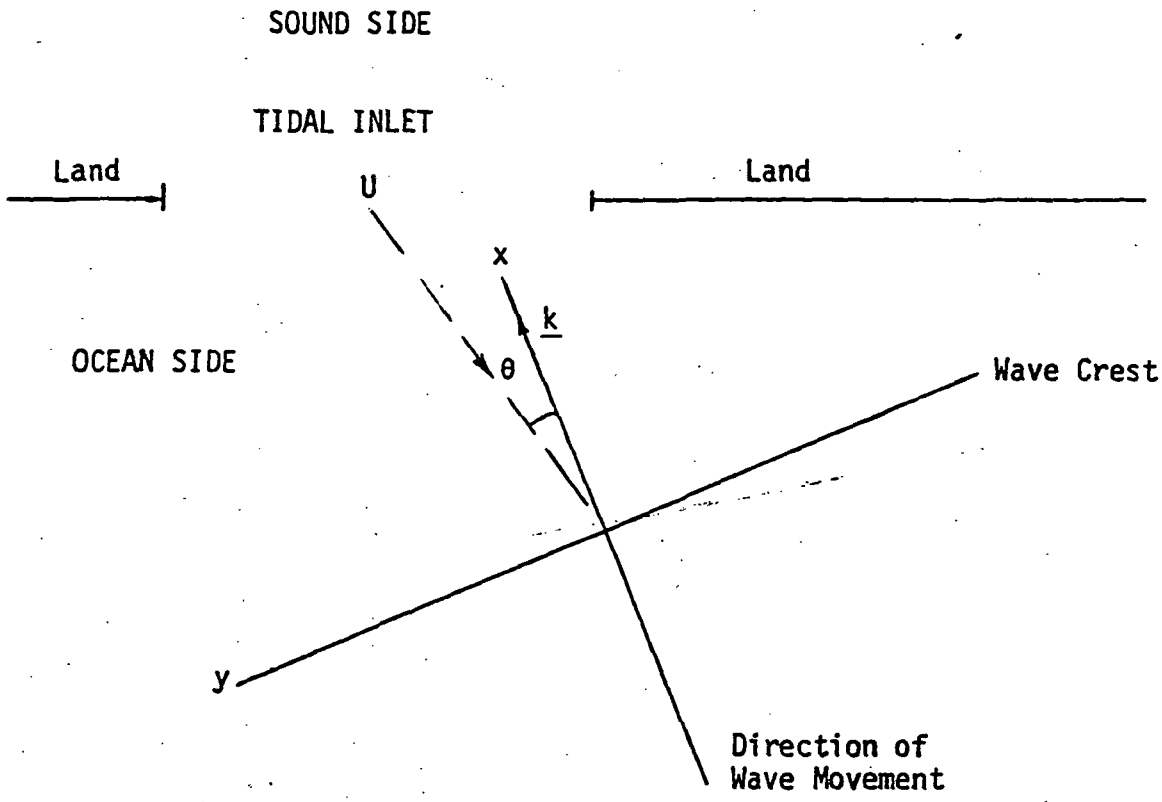

Figure 2.1. Schematic of coordinate system in relation to wave crest, tidal inlet, current and wave movement

therefore, equations 2.3 and 2.4 combined will give

$$\frac{c^2}{c_o^2} - \frac{c}{c_o} - \frac{U}{c_o}\cos\theta = 0 \tag{2.5}$$

which has the solution

$$\frac{c}{c_o} = \frac{1}{2}\left\{1+\left(1+\frac{4U\cos\theta}{c_o}\right)^{1/2}\right\} \tag{2.6}$$

Here only the positive sign for the radical has been retained to reflect physical reality. By combining equations 2.4 and 2.6, the wave number changes can be written as

$$\frac{k}{k_o} = \frac{1}{\frac{1}{4}\left\{1+\left(1+\frac{4U\cos\theta}{c_o}\right)^{1/2}\right\}^2} \tag{2.7}$$

The inverse of this ratio will give the wave length ratio.

By using the irrotational properties of the wave number vector, we have

$$\frac{\partial k\sin\theta}{\partial x} - \frac{\partial k\cos\theta}{\partial y} = 0 \tag{2.8}$$

where the x-axis is parallel to the current direction in this equation. Wave number changes perpendicular to the current direction should be zero, thus,

$$\frac{\partial k\sin\theta}{\partial x} = \frac{\partial k\cos\theta}{\partial y} = 0 \tag{2.9}$$

Hence

$$k\sin\theta = k_o \sin\theta_o \tag{2.10}$$

which is Snell's law of refraction. By combining equations (2.7) and (2.10), the wave refraction equation under current is obtained as

$$\frac{\sin\theta}{\sin\theta_o} = \left\{\frac{1}{2}\left[1+(1+\frac{4U\cos\theta}{c_o})^{1/2}\right]\right\}^2 \qquad (2.11)$$

The wave refraction equation shows that the refraction angle is a function of the initial wave angle relative to the current direction, the initial wave phase speed, and the current speed. When U/c_o is greater then zero, $\sin\theta/\sin\theta_o$ increases with current changes. When the value of U/c_o is less than zero, $\sin\theta/\sin\theta_o$ decreases in an opposing current. The angle of refraction can be obtained from the expanded form of equation 2.11 as

$$\sin^4\theta + \frac{2\,p^2\sin^3\theta_o - 2\sin\theta_o}{(1+p^2\sin^2\theta_o)^2}\sin^3\theta$$

$$+\frac{(1-2p^2)\sin^2\theta_o - 2\,p^4\sin^4\theta_o}{(1+p^2\sin^2\theta_o)^2}\sin^2\theta$$

$$-\frac{2p^2\sin^3\theta_o}{(1+p^2\sin^2\theta_o)^2}\sin\theta + \frac{p^4\sin^4\theta_o}{(1+p^2\sin^2\theta_o)^2} = 0 \qquad (2.12)$$

where $p=U/c_o$. This algebraic expansion can be shown to be the same as Crapper's (1972) wave refraction equation obtained through an independent method using averaged Lagrangian and variational principles.

The wave amplitude can be found by using the wave energy conservation equation:

$$\frac{\partial E}{\partial t} + \frac{\partial}{\partial x_i}\left\{E(U_i+c_{gi})\right\} + \delta_{ij}\frac{\partial U_i}{\partial x_i} = -\varepsilon \qquad (2.13)$$

where E = energy density of the waves per unit area

i,j = indices with values 1,2 corresponding to x,y

U = current velocity

δ_{ij} = excess momentum flux associated with the wave motion

c_{gi} = group velocity of the waves

ϵ = the rate of energy dissipation per unit area

Under the steady state and non-dissipative assumptions, equation 2.13 can be written as

$$\frac{\partial}{\partial x}\left[E\left(U\cos\theta+\frac{1}{2}c\right)\right]+\frac{\partial}{\partial y}\left[EU\sin\theta\right]+\frac{1}{2}E\frac{\partial U\cos\theta}{\partial x}=0 \qquad (2.14)$$

The continuity equation for the current field is

$$\frac{\partial U\cos\theta}{\partial x}+\frac{\partial U\sin\theta}{\partial y}=0 \qquad (2.15)$$

By combining equations 2.14 and 2.15, and through some algebra, we get

$$\frac{E\left(U\cos\theta+\frac{1}{2}c\right)}{c}=\text{const}=\frac{1}{2}E_o \qquad (2.16)$$

Combining equation 2.6 with the energy equation, 2.16, finally gives

$$\frac{E}{E_o}=\frac{1+\left(1+\frac{4U\cos\theta}{c_o}\right)^{1/2}}{\left[\frac{4U\cos\theta}{c_o}+1+\left(1+\frac{4U\cos\theta}{c_o}\right)^{1/2}\right]} \qquad (2.17)$$

This equation indicates how the energy of a wave is modified by the current velocity. Since the energy in a gravity wave is proportional to the square of the amplitude,

$$\frac{a}{a_o}=\left\{\frac{1+\left(1+\frac{4U\cos\theta}{c_o}\right)^{1/2}}{\frac{4U\cos\theta}{c_o}+1+\left(1+\frac{4U\cos\theta}{c_o}\right)^{1/2}}\right\}^{1/2} \qquad (2.18)$$

Associated with the wave amplitude is the wave slope or the wave steepness, s, defined as the ratio of the wave height to the wave length:

$$s = \frac{H}{L} = \frac{ak}{\pi} \tag{2.19}$$

Thus

$$\frac{s}{s_o} = \frac{1}{\left\{\frac{1}{2} + \frac{1}{2}\left(1 + \frac{4U\cos\theta}{c_o}\right)^{1/2}\right\}^2} \cdot \left\{ \frac{1 + \left(1 + \frac{4U\cos\theta}{c_o}\right)^{1/2}}{\frac{4U\cos\theta}{c_o} + 1 + \left(1 + \frac{4U\cos\theta}{c_o}\right)^{1/2}} \right\}^{1/2} \tag{2.20}$$

With all the equations of wave characteristics given, the values of the various quantities can be calculated. The calculation starts with the equation of wave refraction given in the expanded form. For given θ_o and U/c_o values, the refraction angle changes are shown in Figure 2.2. The resulting refracted angle values are then applied to equation 2.17 to solve for the energy changes under current as shown in Figure 2.3; to equation 2.18 to solve for amplitude changes as shown in Figure 2.4; to equation 2.20 to solve for the wave slope changes as shown in Figure 2.5; to equation 2.7 to solve for wave number changes as shown in Figure 2.6; and to equation 2.6 to solve for the phase velocity changes as shown in Figure 2.7.

As the wave propagates against current, the wave slope keeps increasing. The upper limit of the steepness can not exceel 1/7 as shown by Michell (1893). Using this criteria, we can establish a stability curve to predict the breaking conditions of waves. This limit is shown in Figure 2.8.

2.3 The Probability Distribution Function for Random Waves

The calculations presented in the previous section apply to simple wave trains only. In the natural environment, wave fields are always random in amplitude and direction; therefore, a complete description of the wave problem should be in terms of directional wave spectra. However, practical capability limited the available experimental data to a simple wave

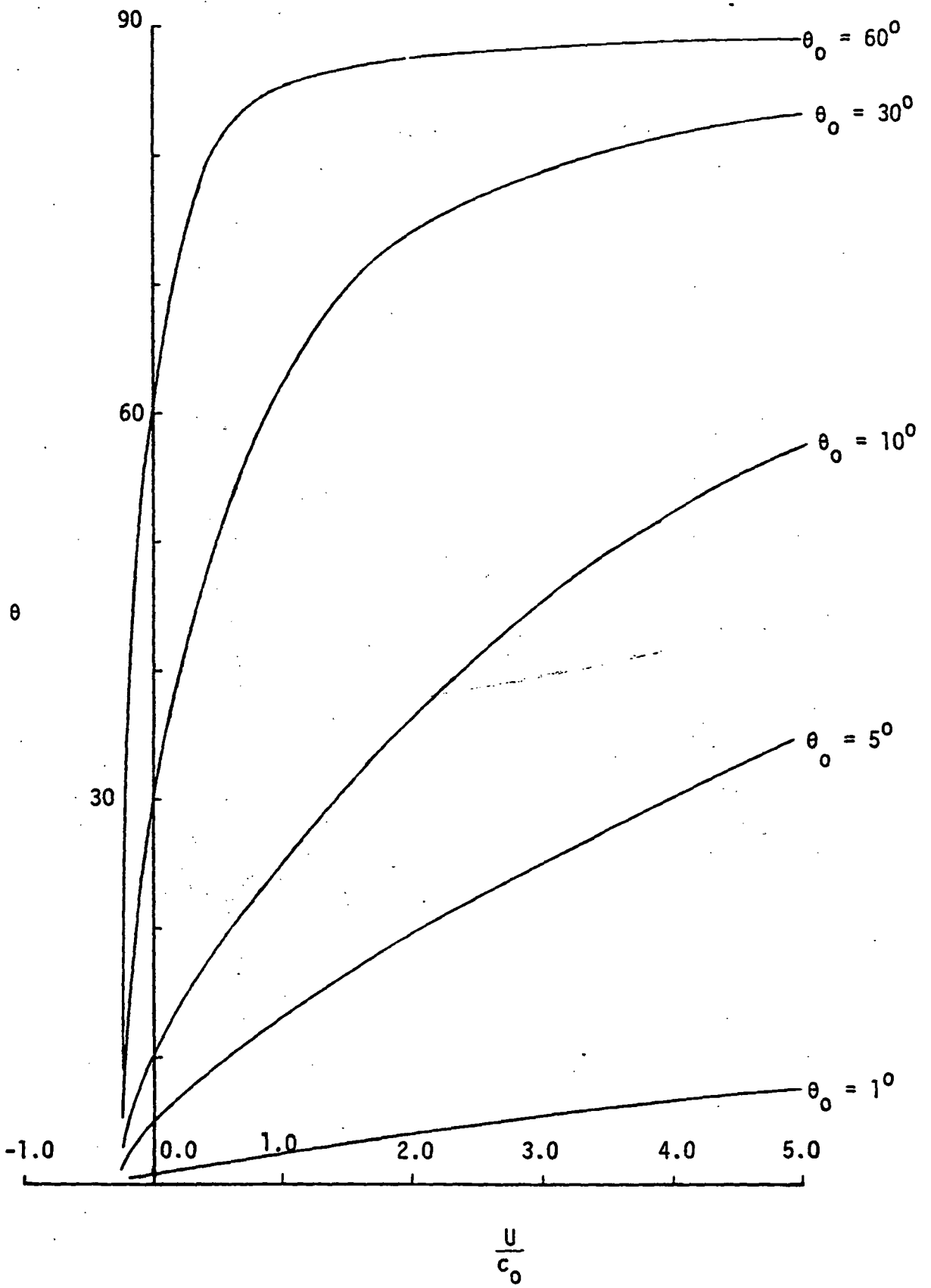

Figure 2.2. Wave refraction angle θ (degrees) versus velocity ratio U/c_o

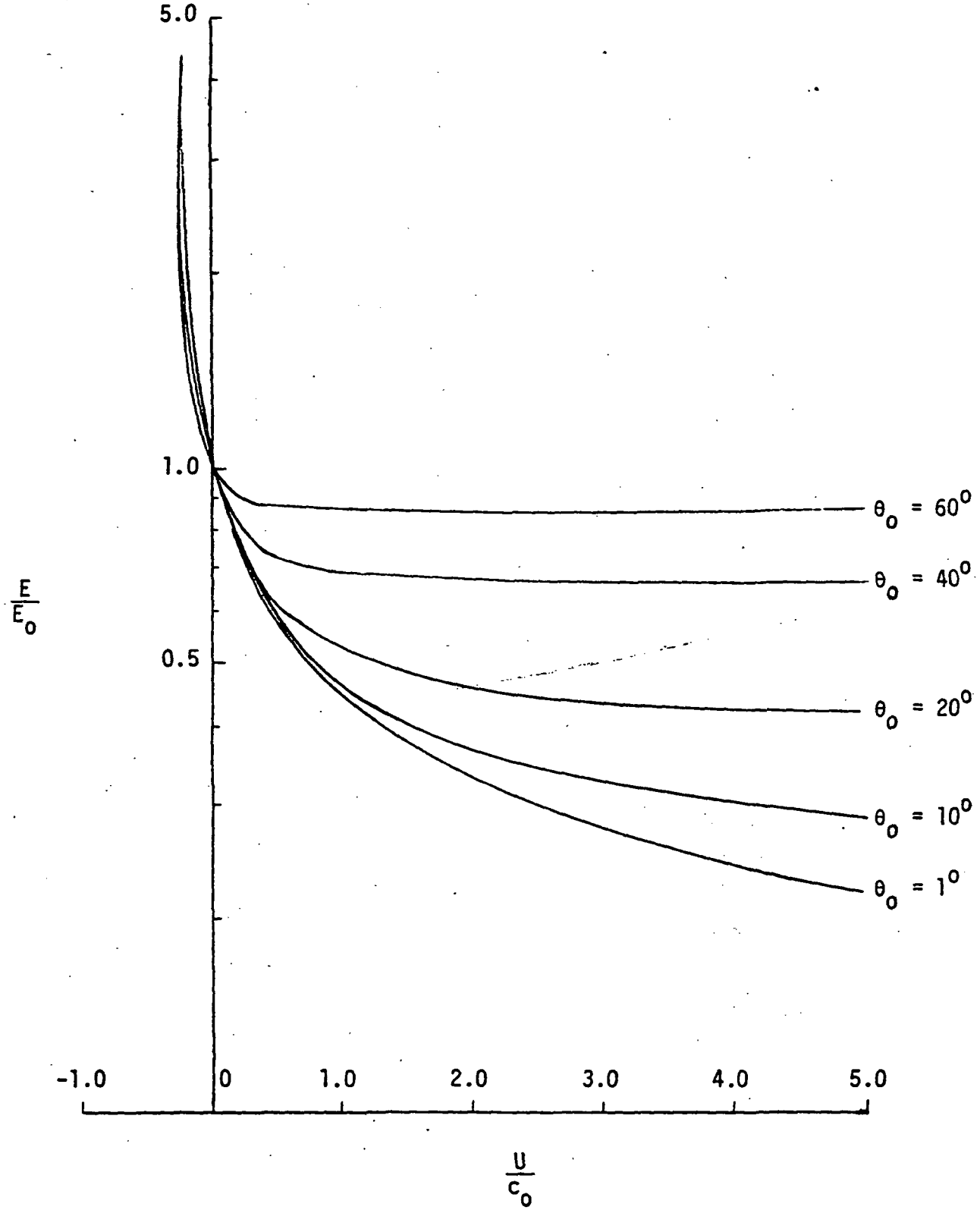

Figure 2.3. Wave energy ratio E/E_o versus velocity ratio U/c_o

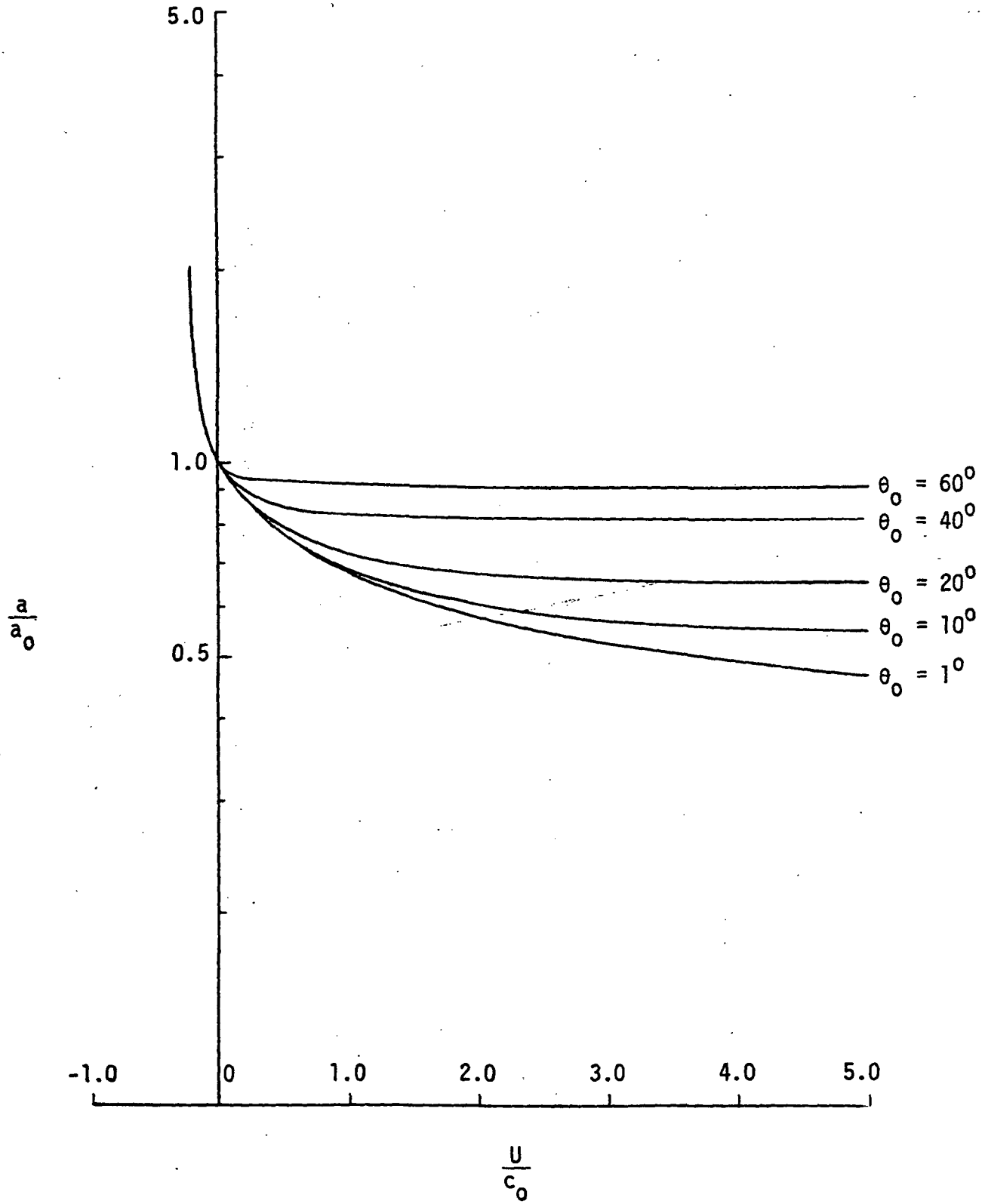

Figure 2.4. Wave amplitude ratio a/a_o versus velocity ratio U/c_o

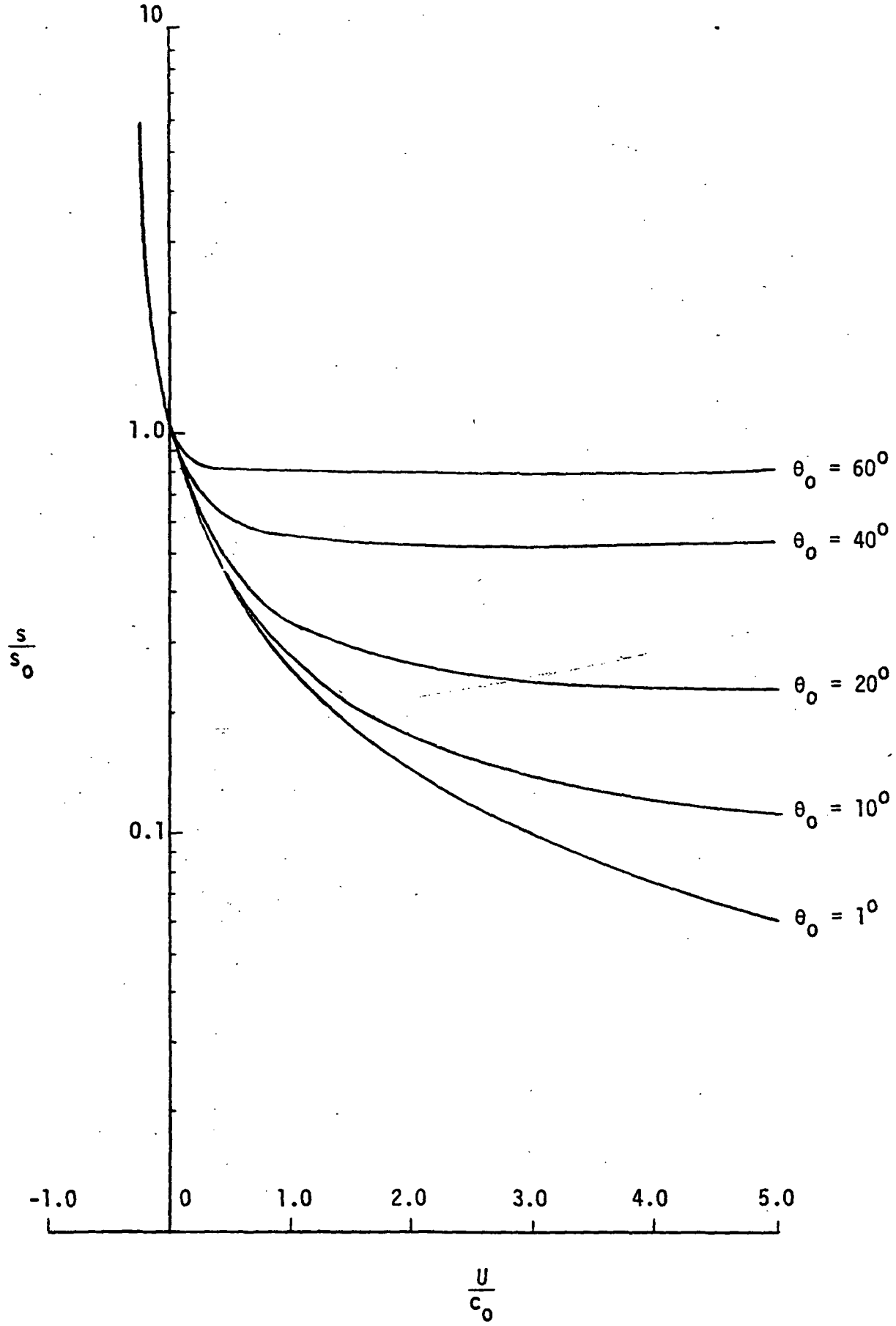

Figure 2.5. Wave slope ratio s/s_o versus velocity ratio U/c_o

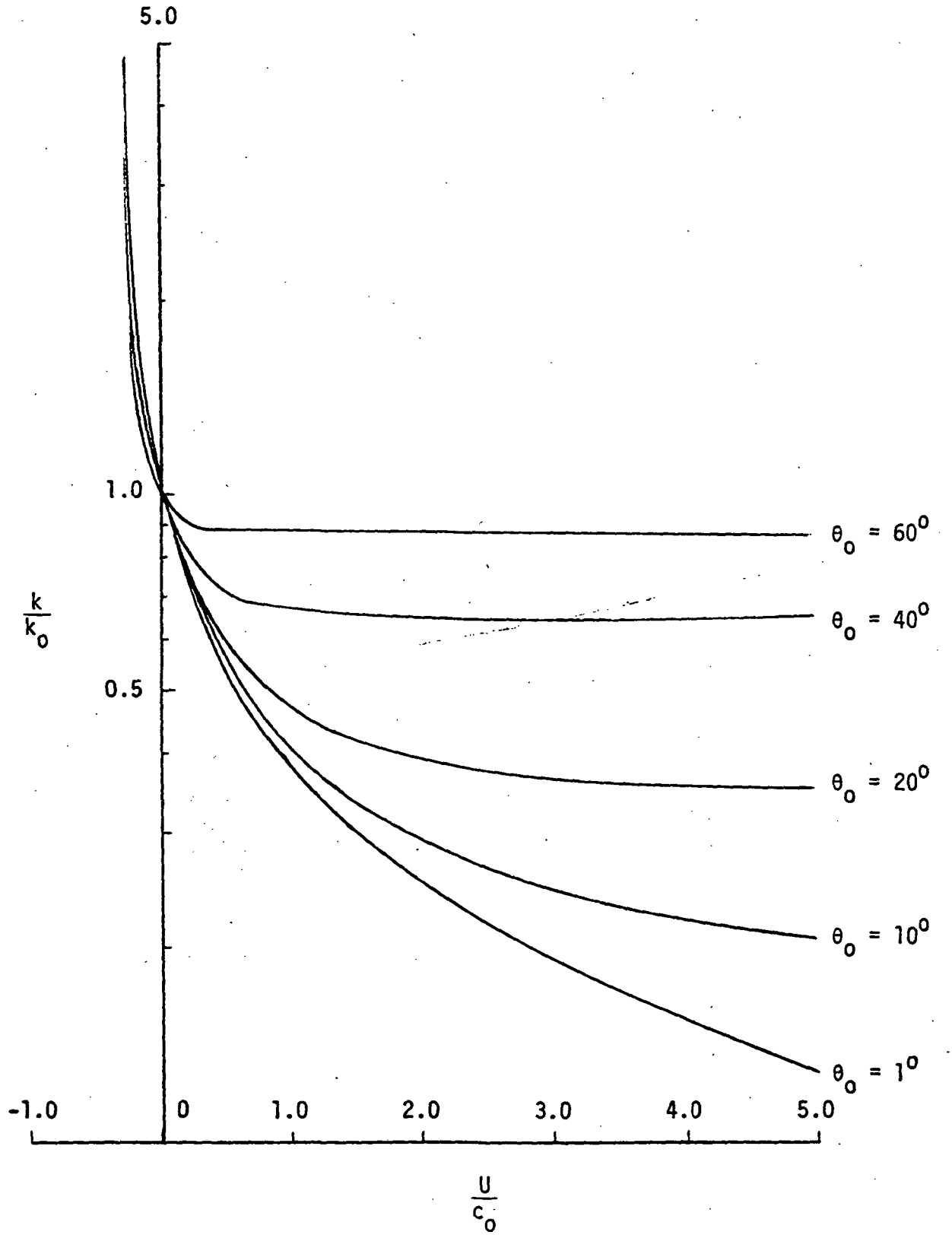

Figure 2.6. Wave number ratio k/k_o versus velocity ratio U/c_o

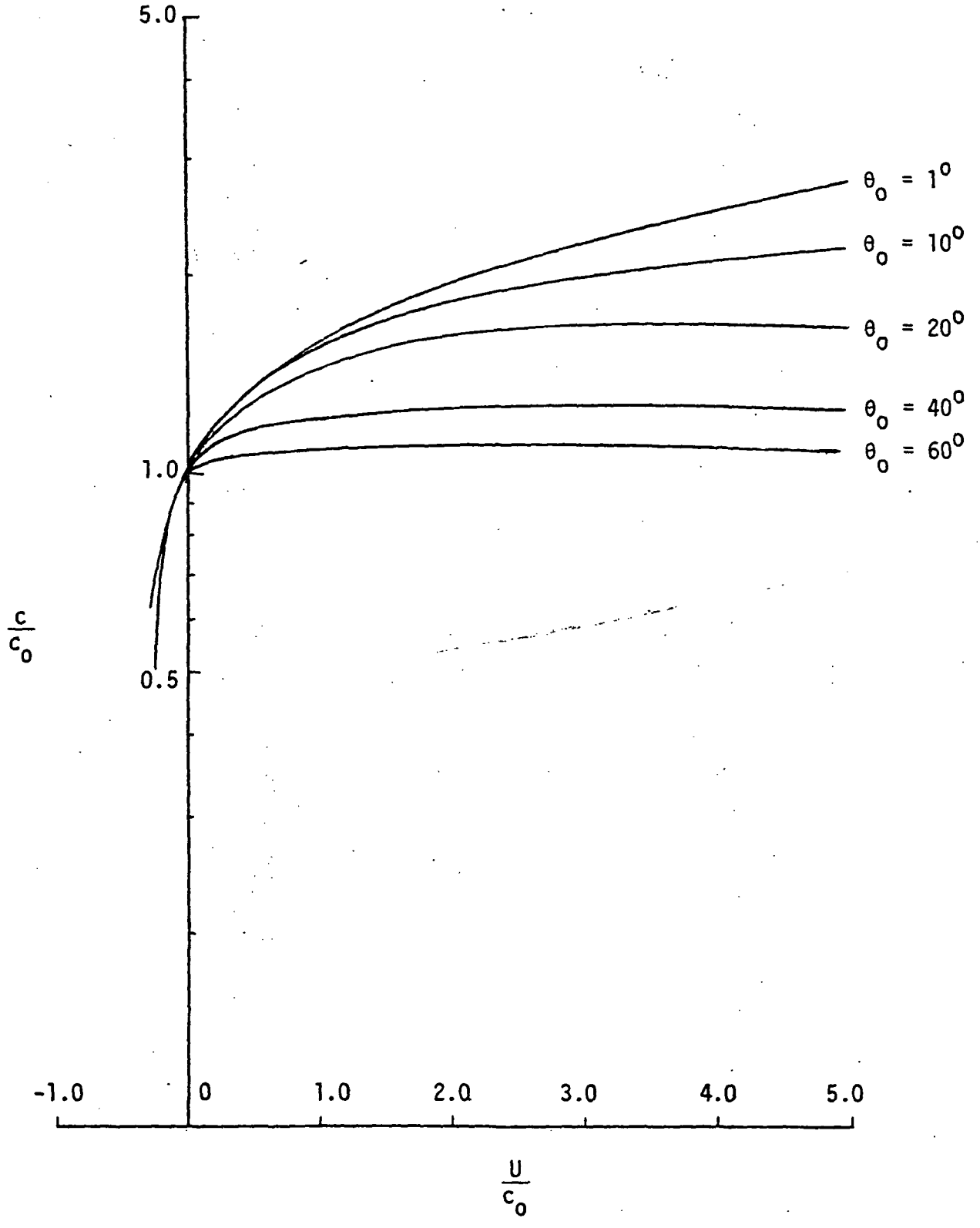

Figure 2.7. Wave phase velocity ratio c/c_o versus velocity ratio U/c_o

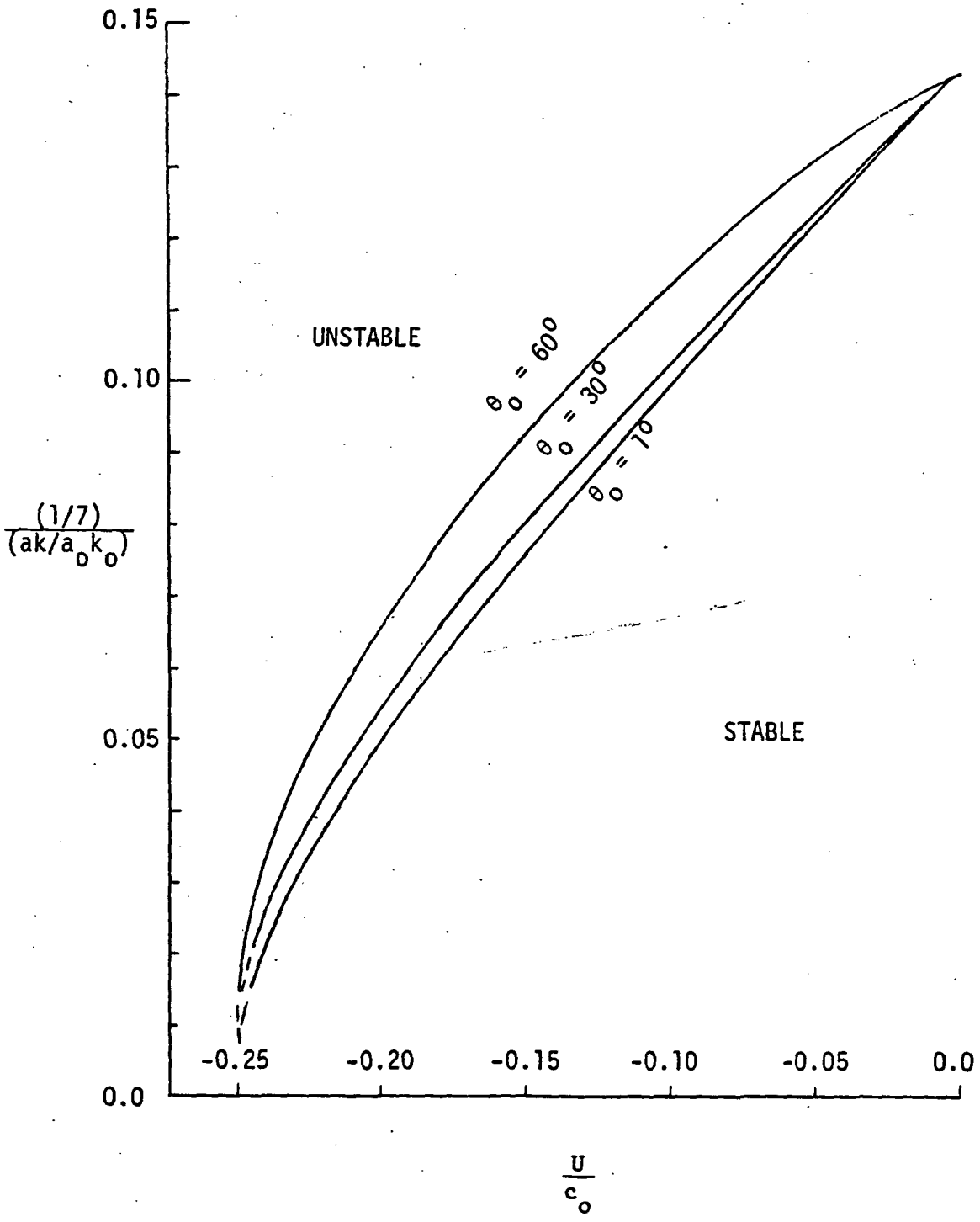

Figure 2.8. Stability ratio $(1/7)/s/s_o)$ versus velocity ratio U/c_o

frequency spectrum only. Consequently a number of very attractive properties of waves such as the changes in wave number, phase speed, direction et al. can not be fully utilized for measurements of current conditions.

With this limitation, other statistical characteristics in frequency space should be considered in more detail. By using the energy equations, the changes in the energy spectra in frequency space can be calculated. This has been discussed in previous reports (Huang, et al. 1974). In addition to the spectra, the probability density function of the surface elevation offers another measurement of the influence of the current on wave fields. Another practical advantage of studying the probability density function is that the quantities are measurable by radar techniques (see, for example, Yaplee et al. 1971).

Both theoretical and field studies show that the probability density function of the surface elevation of a wave field is approximately Gaussian. Thus

$$P(\zeta) = (2\pi\overline{\zeta^2})^{-1/2} \exp(-\frac{1}{2}\zeta^2/\overline{\zeta^2}) \qquad (2.21)$$

where ζ stands for the surface elevation measured from the mean sea level, and the over bar indicates averages. When non-linear mechanisms are included, the density function can be approximated by a Gram-Charlier series with the leading term still Gaussian as shown by Longuet-Higgins (1960). Since all the non-linear interactions are weak in nature, if we neglect the non-linear effects and accept the first order approximation, the probability density function of the surface elevation will then depend on $\overline{\zeta^2}$ which is controlled by the current-wave interactions under a given wind condition.

Two cases of current conditions are considered to show the influence of current on the density function. The first case involves variable currents in one dimension only. As an example consider the Gulf Stream as a uniform current which is a function of the variable x, measured perpendicular to the direction of current flow. The Gulf Stream is confined to a particular region of x space. The energy conservation equation for this case is:

$$E(U + \frac{c}{2})c = \text{constant} \quad , \tag{2.22}$$

where E is the total wave energy; U, the current velocity, and c, the phase speed of the waves. The changes in the spectral function are given by Huang *et al.* as

$$\phi(n) = \frac{4\phi_o(n)}{[1 + (1 + \frac{4Un}{g})^{1/2}]\ [(1 + \frac{4Un}{g})^{1/2} + (1 + \frac{4Un}{g})]} \quad , \tag{2.23}$$

where n is the frequency and $\phi_o(n)$ is the spectral function when the current equals zero. Various forms of $\phi_o(n)$ can be used in equation (2.23). For the present discussion the Kitaigordoskii-Moskowitz-Pierson spectrum is adopted, i.e.,

$$\phi_o(n) = \frac{\beta g^2}{n^5} e^{-(\frac{n_o}{n})^4} \tag{2.24}$$

where $n_o = \frac{g}{w}$ with w standing for wind speed. Since the wave energy spectra are modified by the current, so is $\overline{\zeta^2}$ which equals

$$\overline{\zeta^2} = \int_o^{n_c} \phi(n)\,dn \tag{2.25}$$

where n_c is the cut-off frequency of the wave spectrum taken as that of a wave 30 cm in length in the present study.

The second case deals with converging or diverging currents with continuity equation as

$$\frac{\partial U}{\partial x} + \frac{\partial U}{\partial y} = 0 \quad . \tag{2.26}$$

Under this condition, the equation for energy conservation is

$$\frac{E(U + \frac{1}{2}c)}{c} = \text{const}, \tag{2.27}$$

and the spectral function becomes

$$\phi(n) = \frac{\phi_o(n)\ [n + (1 + \frac{4Un}{g})^{1/2}]}{1 + (1 + \frac{4Un}{g})^{1/2} + \frac{4Un}{g}} \quad . \tag{2.28}$$

Again the changes in $\phi(n)$ are reflected in $\overline{\zeta^2}$ and the probability density functions. The results are shown in Figures 2.9, 2.10, 2.11, and 2.12.

These results indicate that the probability density functions are sensitive to whatever causes changes in $\overline{\zeta^2}$. This is true even when the higher order expansion terms in Gram-Charlier series are considered. In the open ocean, mechanisms that will change $\overline{\zeta^2}$ substantially, are, of course, winds and major currents. However, since we lack more detailed knowledge of the generation of waves by wind, it is not easy to utilize these properties as a means to measure wind velocity over the ocean, because swells from previous storms will also change $\overline{\zeta^2}$.

On the other hand, current-wave interaction is more definite and is a first order effect. Furthermore, since the change depends on relative values of currents, it is less susceptible to the error in establishing an absolute relationship as required in wind wave generation studies. Under normal conditions a wind system will cover an area substantially larger than the scale of waves and thus will provide a homogeneous field for wave action. In an inlet or a river mouth for example, the local flow will generate a non-uniform velocity field over a homogeneous wave field. Consequently, the waves will interact and change characteristics depending on the flow conditions. Such changes can be detected easily from the probability density function, but further study is needed to put this approach on a sound quantitative basis.

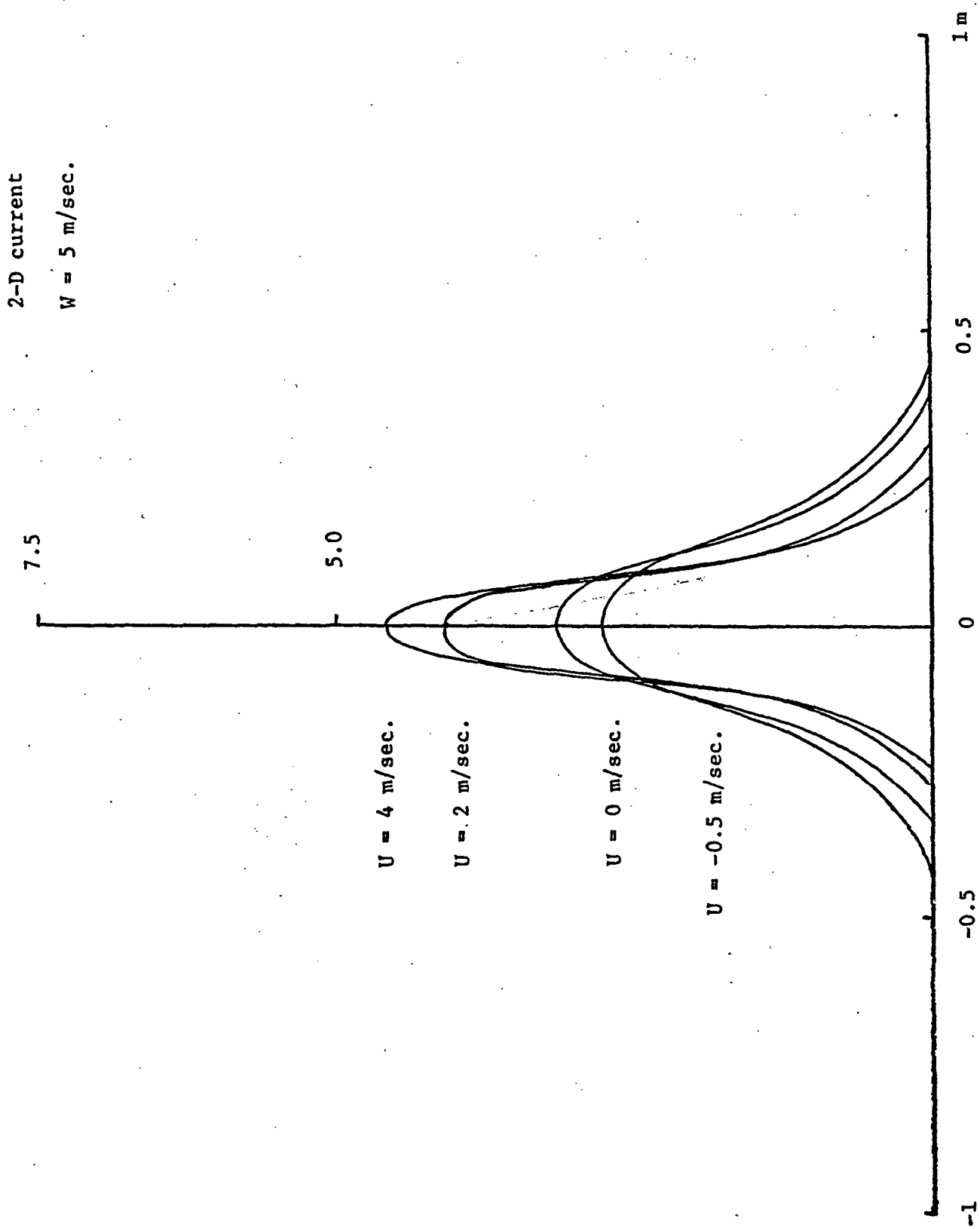

Figure 2.9. Probability density distribution curves for surface elevation; W = 5 m/sec.

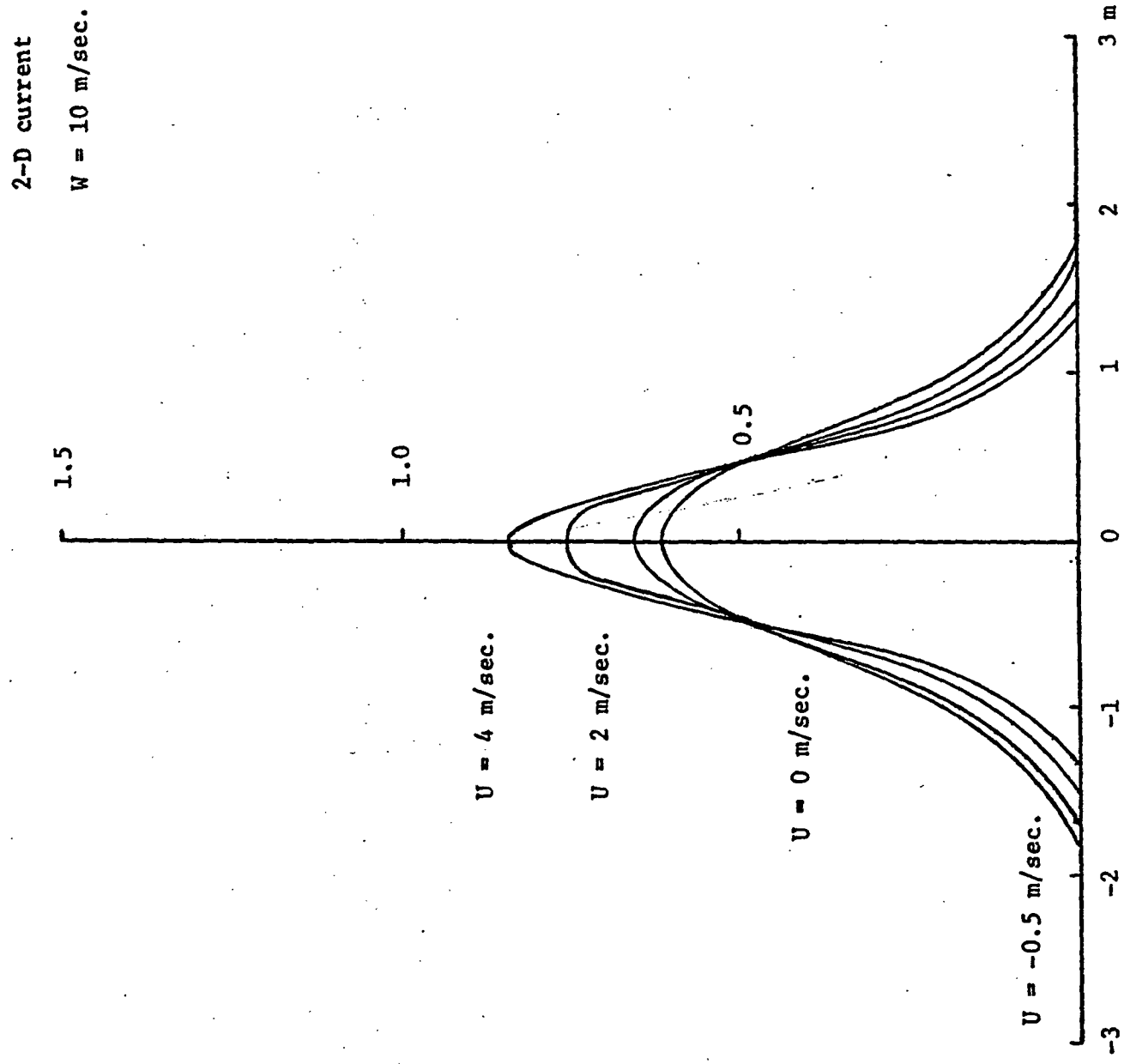

Figure 2.10. Probability density distribution curves for surface elevation; W = 10 m/sec.

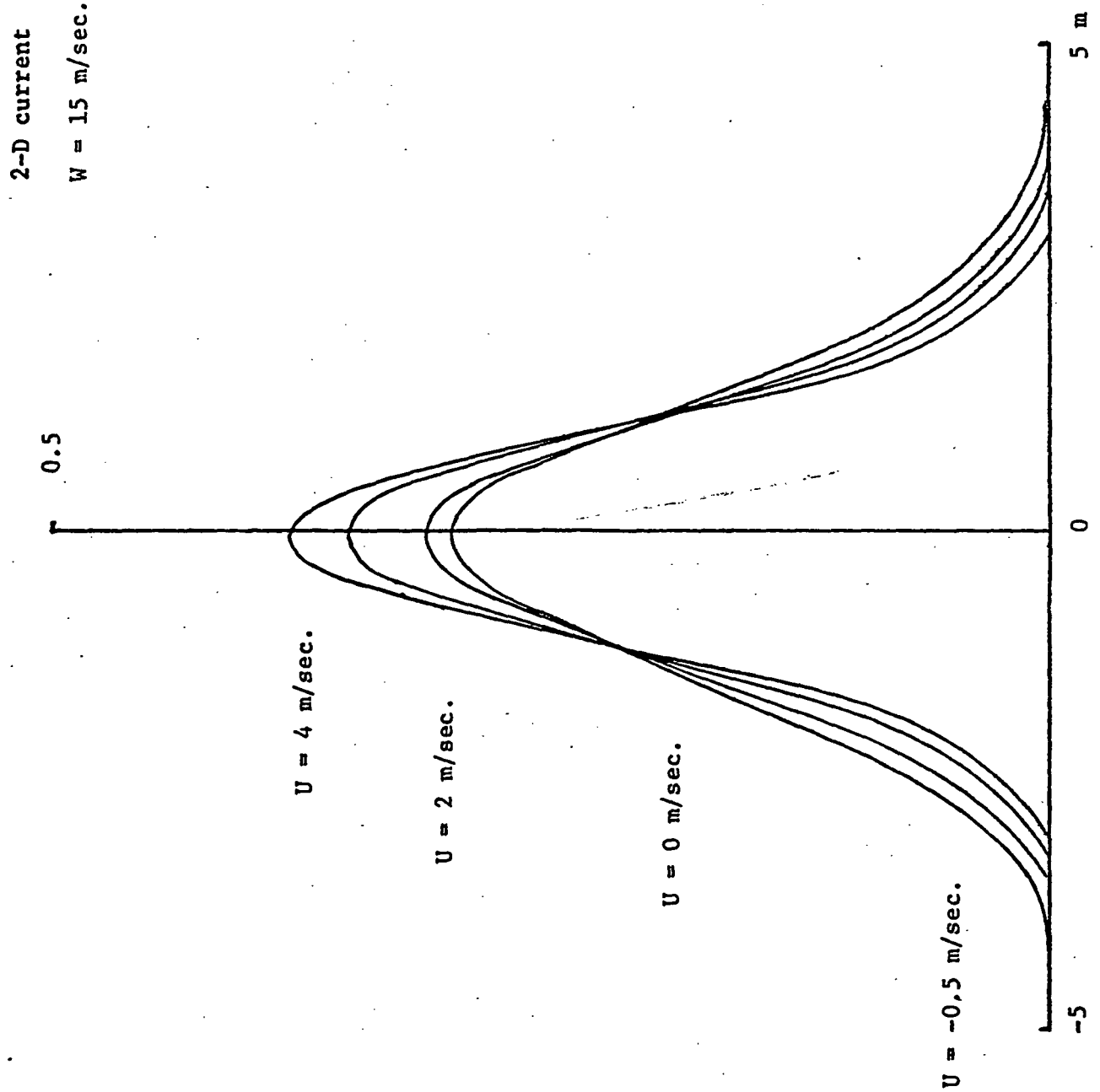

Figure 2.11. Probability density distribution curves for surface elevation; W = 15 m/sec.

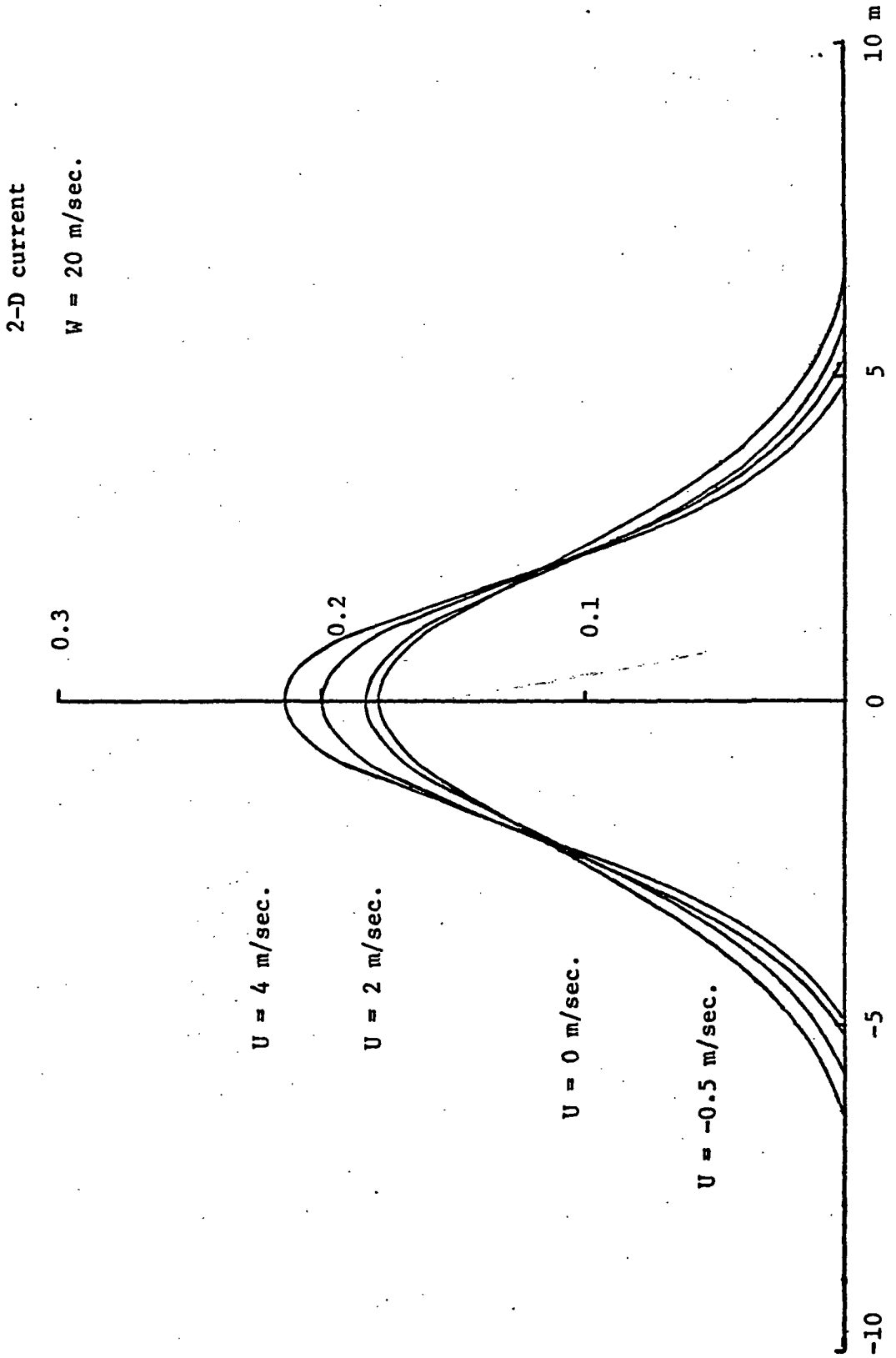

Figure 2.12. Probability density distribution curves for surface elevation; W = 20 m/sec.

3.0 FIELD STUDIES

3.1 Introduction

The purpose of the field study was to conduct an experimental program to establish the feasibility of using remotely sensed wave observations to detect and measure ocean currents. Such a field test program must be supported by in-situ, ground truth measurements. The presence of a field team from North Carolina State University making physical oceanographic measurements at Hatteras Inlet, on the Outer Banks of North Carolina, suggested that remotely sensed wave observations made at this location during the North Carolina State field period might provide the basis of a fruitful test of the theory presented in Part II of this report.

The initial plan called for four aircraft flights (two at ebb and two at flood tides) carrying a laser profilometer and the NRL nanosecond radar. The NRL radar was not available during the planned flight periods and scheduling difficulties with the aircraft resulted in only three test flights. Equipment malfunctions on two of the three test flights flown resulted in useable data being restricted to the flight of July 15, 1974. This data forms the basis for the field study.

Figure 3.1 illustrates the location of Hatteras Inlet on the Outer Banks of North Carolina. The inlet connects Pamlico Sound to the Atlantic Ocean. Figure 3.2 is a more detailed drawing of the area and clearly shows the presence of the small islands near the mouth of the inlet. These islands produce an extremely complicated water flow pattern which make Hatteras Inlet a less than ideal experimental site. The presence of gently sloping beaches on the ocean side of the bank further complicate the data interpretation by introducing the possibility of shallow water effects which are not accounted for in the throry. The reason for the selection of Hatteras for the experimental test site was primarily to take advantage of the physical oceanographic observations which could be provided by the North Carolina State University field investigation.

3.2 Collection of Ground Truth Data

The physical oceanographic team from North Carolina State University made current measurements at Hatteras Inlet from the 9th to the 16th of July, 1974. These ground truth activities can be described as follows.

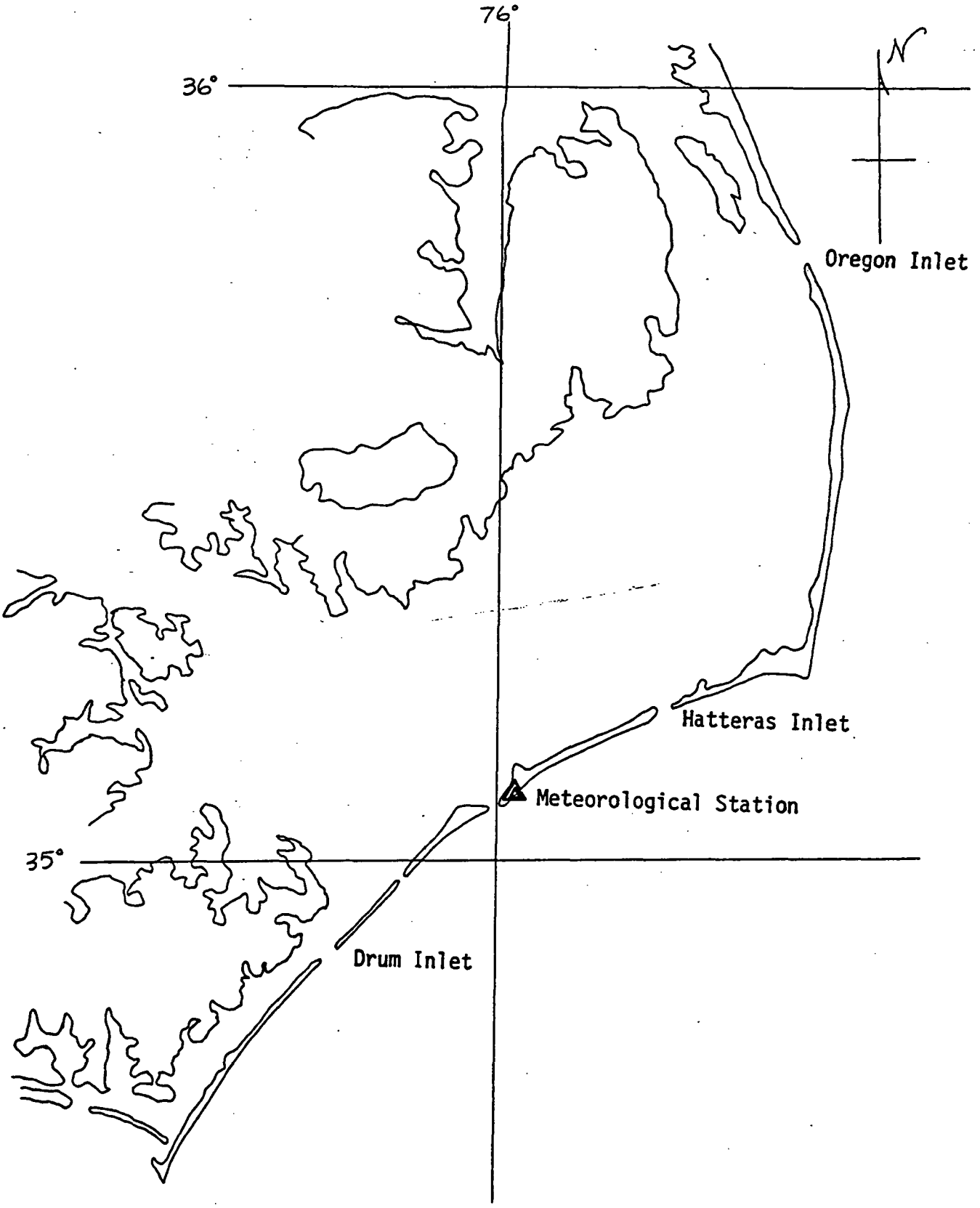

Figure 3.1. Geographic location of Hatteras Inlet

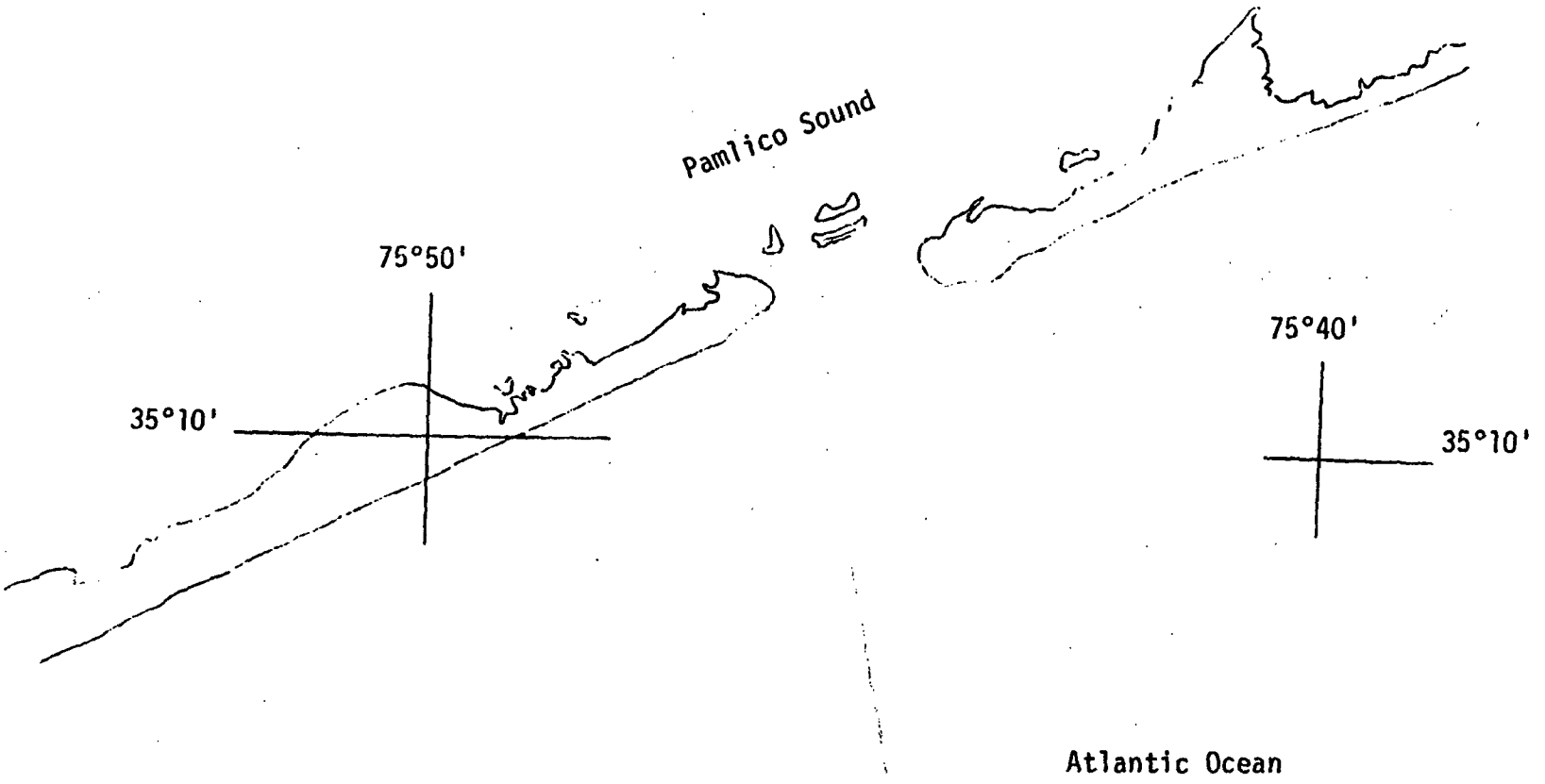

Figure 3.2. Details of Hatteras Inlet, N. C.

A. Bathymetrical Survey

A portable fathometer was used from a 16 ft. boat equipped with an outboard motor, to make the bathymetrical survey. The paths of the survey tracks near the Inlet are shown in Figure 3.3. Though the width of the inlet is about 8000 ft., the maximum depth is only 25 ft. The depth profiles obtained are shown in Figures 3.4 and 3.5. The survey results indicated the shallowness and the complicated nature of the bottom features of the Inlet. The Inlet is not stable; dredging and erosion change the Inlet geometry continuously. A decision was made at this point to complete all measurements as quickly as possible; definitely within the summer and fall before the onset of winter storms and resulting drastic changes in Inlet conditions.

B. Tracking Floating Buoys

Three dozen disposable buoys were prepared for measurement of the Lagrangian surface current in the Inlet area because the boat used was too small to be safely operated there. The buoys were 2' cubic sealed cardboard boxes painted bright orange and weighted with sand to make the boxes slightly buoyant so that only one-half of a box would be above the water surface. Two transit stations were established on one of the islands facing the ocean at the Inlet mouth as shown in Figure 3.3. The distance between the stations was 1,181 ft., thus providing a trangulation baseline sufficient for determining the position of the buoys. A total of 30 buoys were released at various times and positions and tracked as they moved through the Inlet. Results of measurements on 15 July are shown in Figure 3.6. Surface current values deduced from buoy motion are shown on the figure.

C. Current Meter Measurements

A total of twelve current meters were deployed by the North Carolina State University Marine Science team. Due to limitations of the meters none was placed in the Inlet itself. The locations of the two nearest to the Inlet mouth, that were

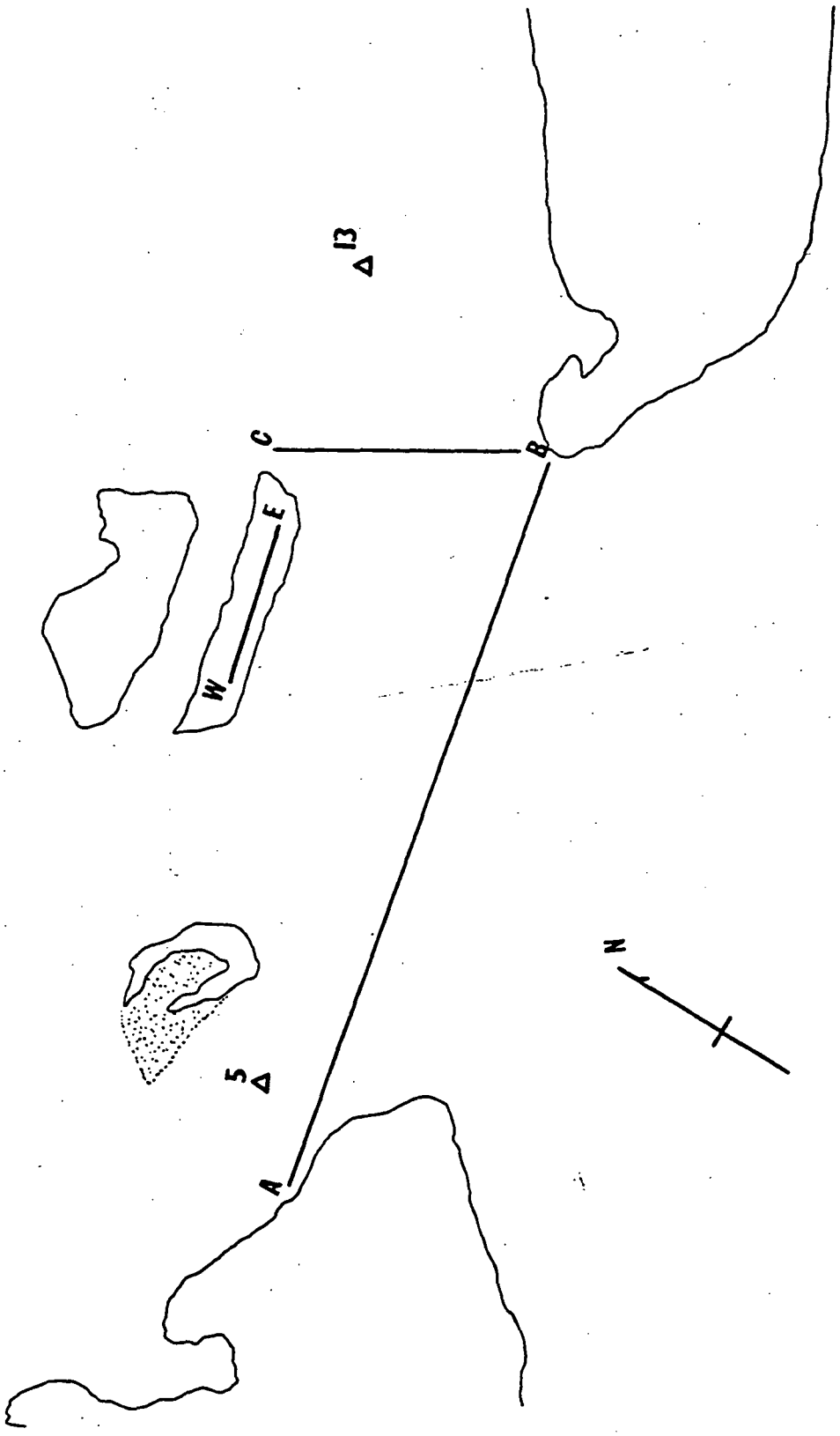

Figure 3.3. Map of Bathymetric Survey paths AB, BC; Transit Stations WE; and current meter locations Mark 5 Mark 13

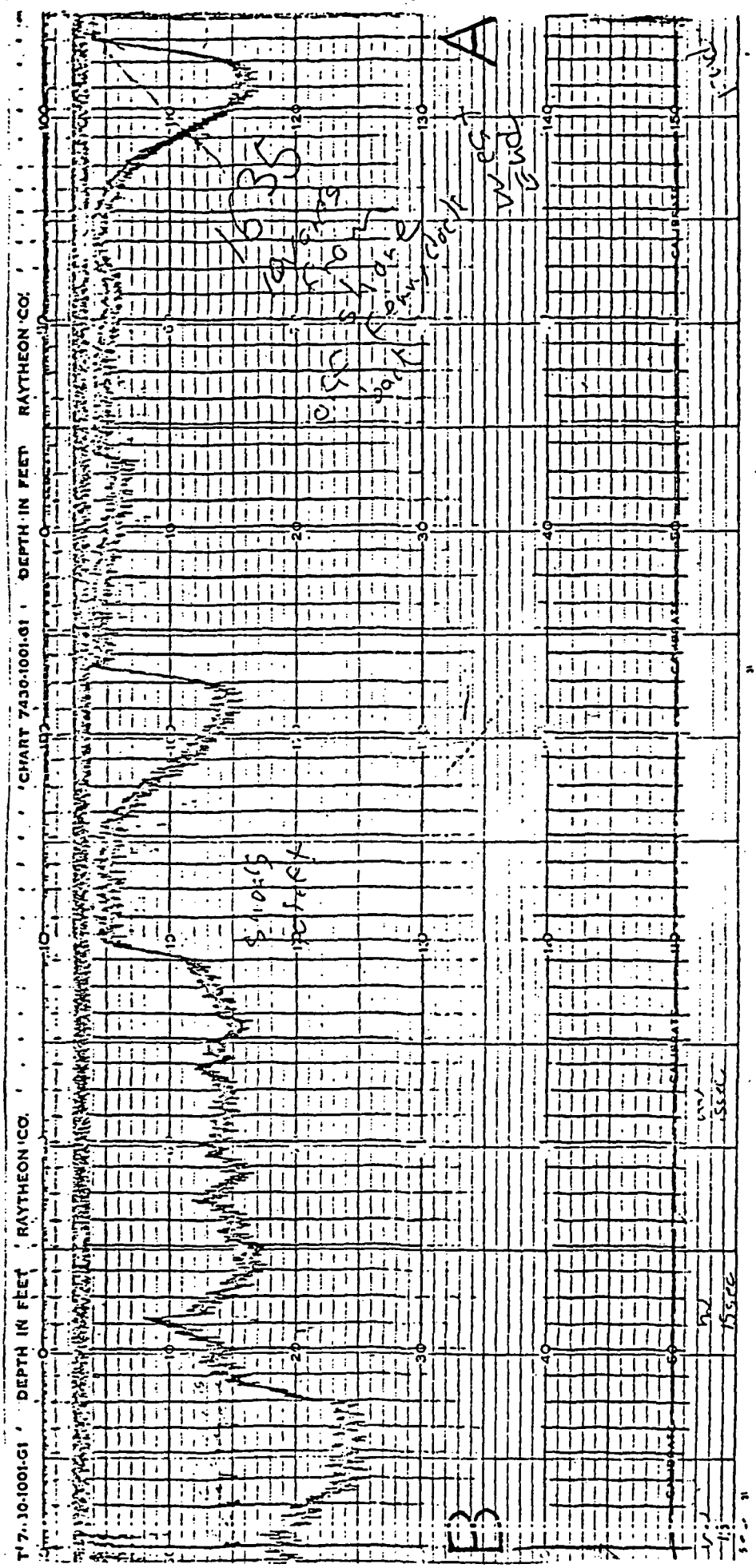

ORIGINAL PAGE IS
OF POOR QUALITY

Figure 3.4. Bathymetric profile along A-B on Figure 3.3

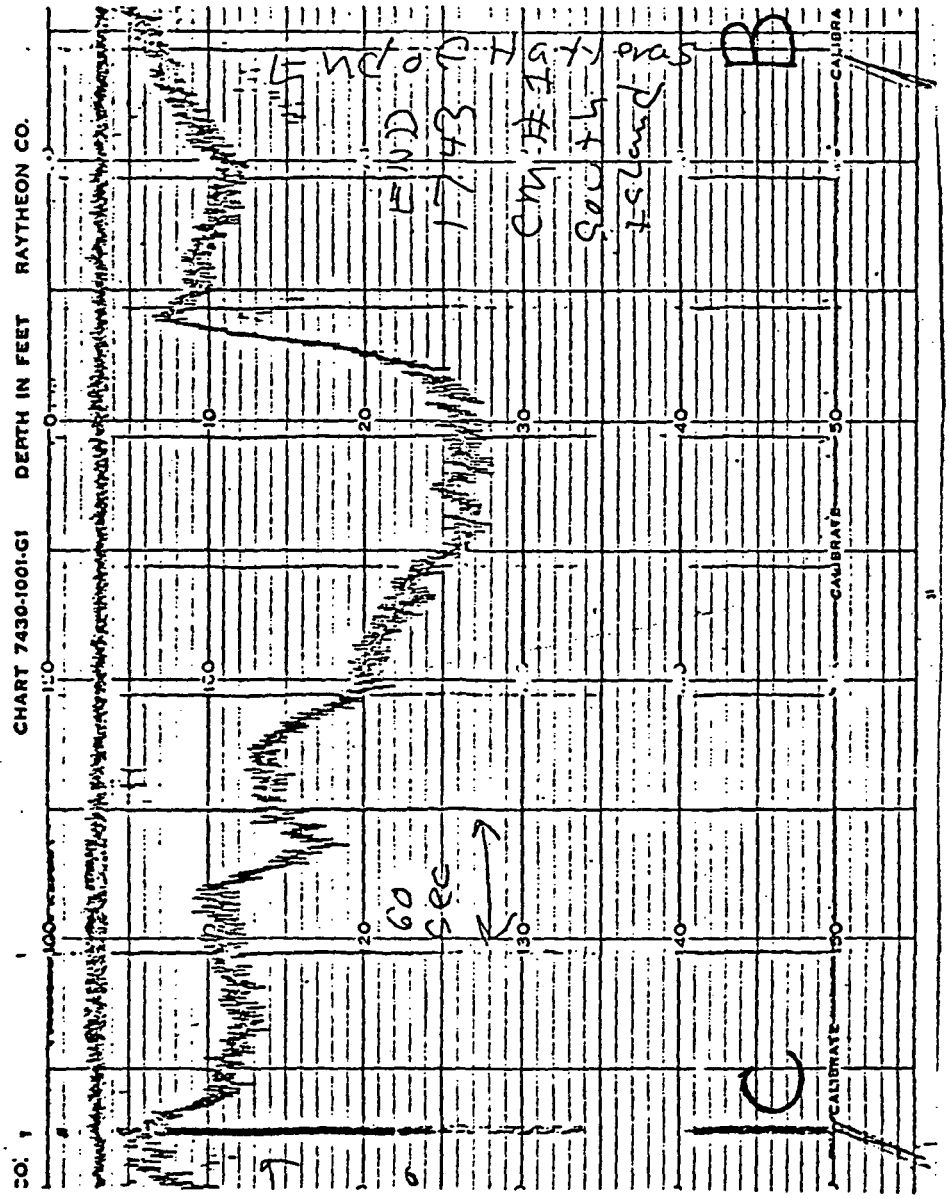

Figure 3.5. Bathymetric profile along B-C on Figure 3.3

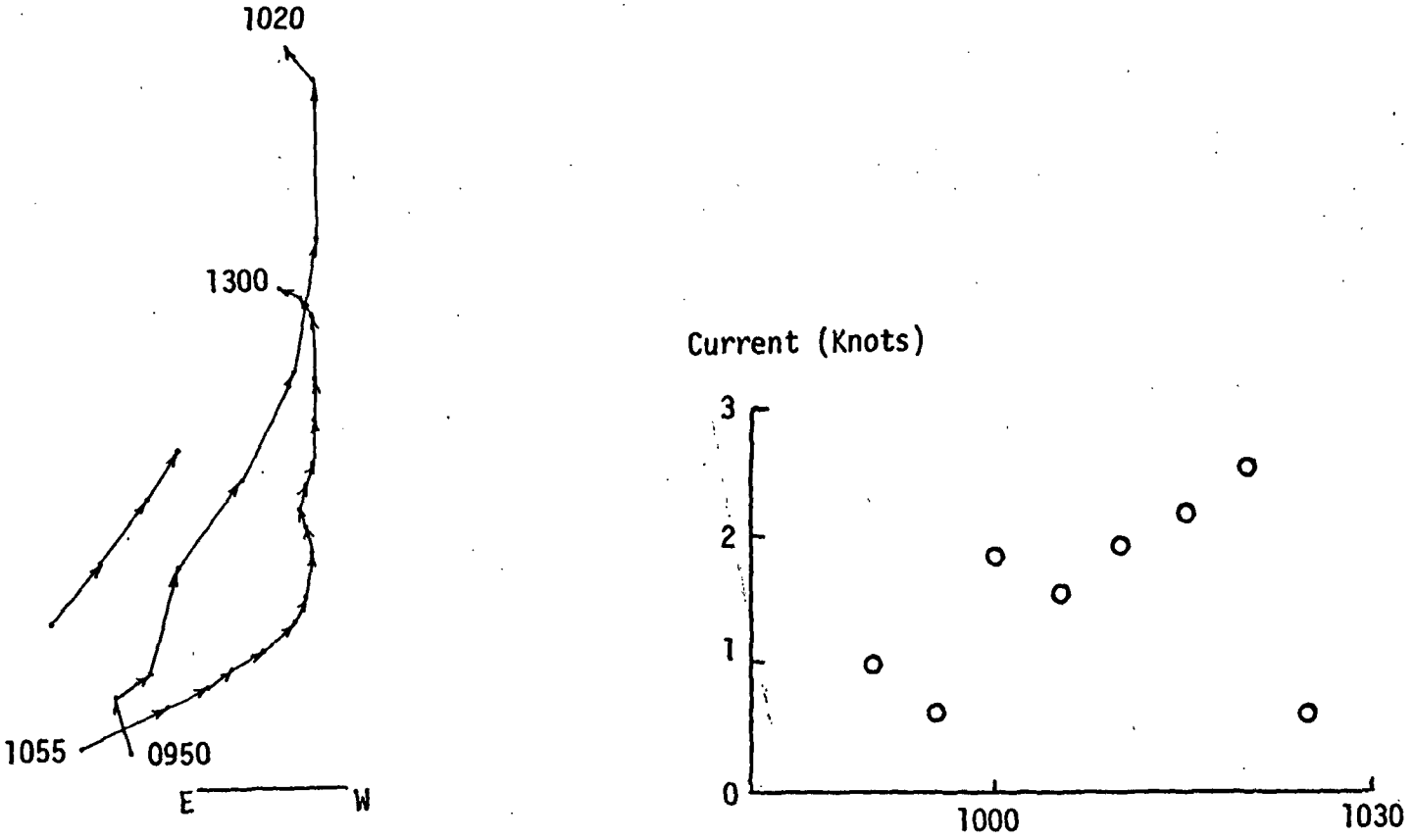

Figure 3.6. Buoy tracing records on July 15, 1974

most important to this study are shown in Figure 3.3. The current meters used were General Oceanics Model 2010 film recording meters. These instruments operate on the principle that a buoyant wand tethered at one end will deflect into the current stream at an angle and direction that are functions of the current speed and direction. The sensing and recording of this deflection yields information that can be readily translated into current speed and direction data. Accuracies of measurements of current speed is $\pm$ 3%, and direction is $\pm 5^{o}$. The current meters were attached to 90 lb. weights sunk to the bottom. The meters were positioned 9 ft. above the bottom. Current magnitudes and directions from these two stations are shown in Figures 3.7 and 3.8. These values are comparable to the ones obtained by the surface buoys discussed in the previous paragraph.

D. Weather Data

A portable weather station was established 20 miles southwest of the Inlet at a Coast Guard Station. Standard meteorological parameters were recorded continuously. Figure 3.9 shows the wind data during the time of the buoy observations and the current meter recordings. The wind data indicated that during the flight time on July 15, 1974, the wind was coming from the direction perpendicular to the axis of the Inlet, thus the locally generated waves also moved in that direction. The wind speed was around 15 knots which generated a sea state too low to be tracked continuously by the laser profilometer. This was not the most favorable condition to conduct the flight test, but due to problems in scheduling the aircraft for alternate dates, the aircraft experiment was conducted.

3.3 The Aircraft Experiment

A flight test plan was drawn up for the acquisition of data on wind-wave height from one of the NASA Wallops Flight Center C-54 aircraft, using a laser profilometer as the primary and the nanosecond radar as the secondary source of data. The date scheduled for the first

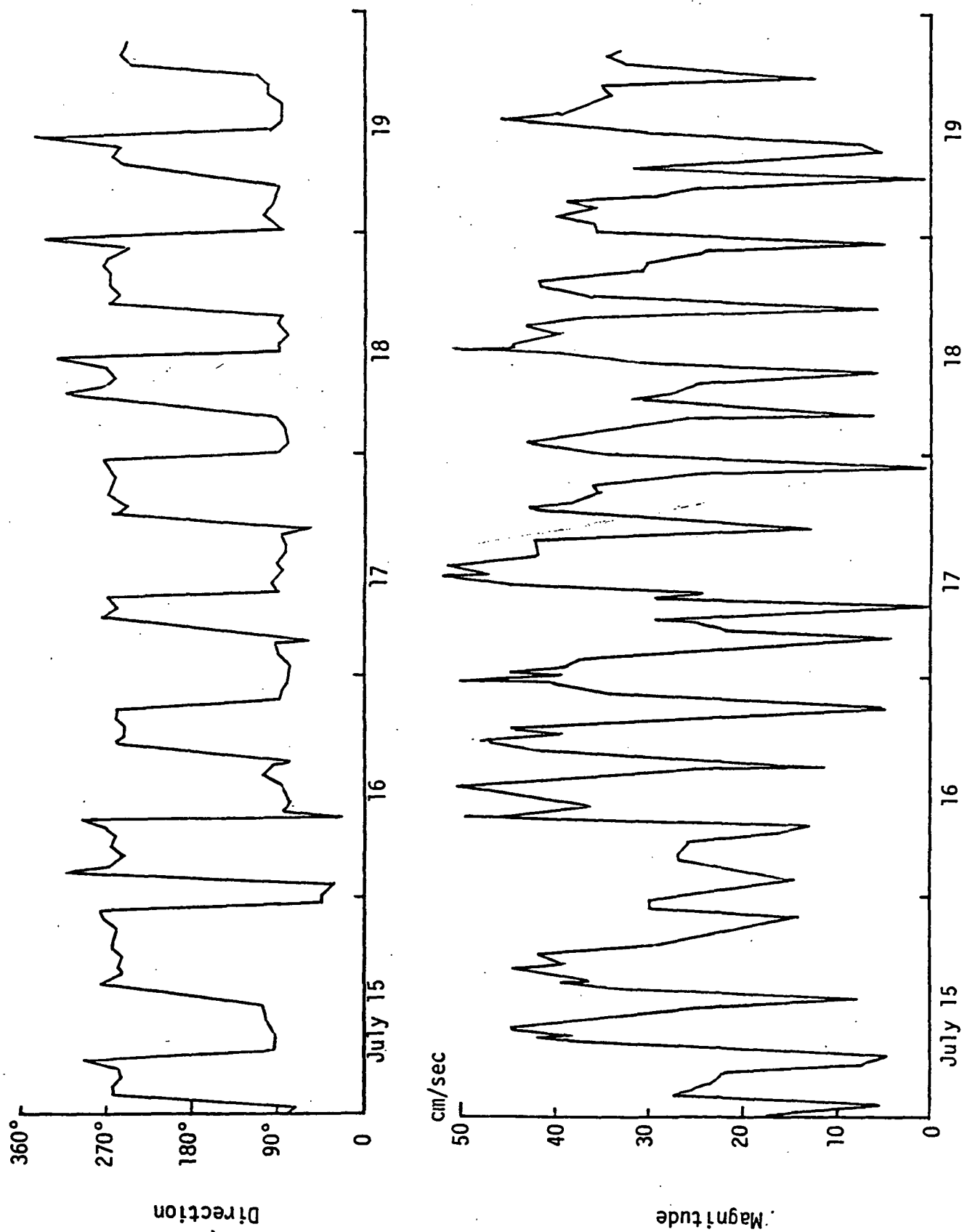

Figure 3.7. Current meter data at Mark 5 on Figure 3.3

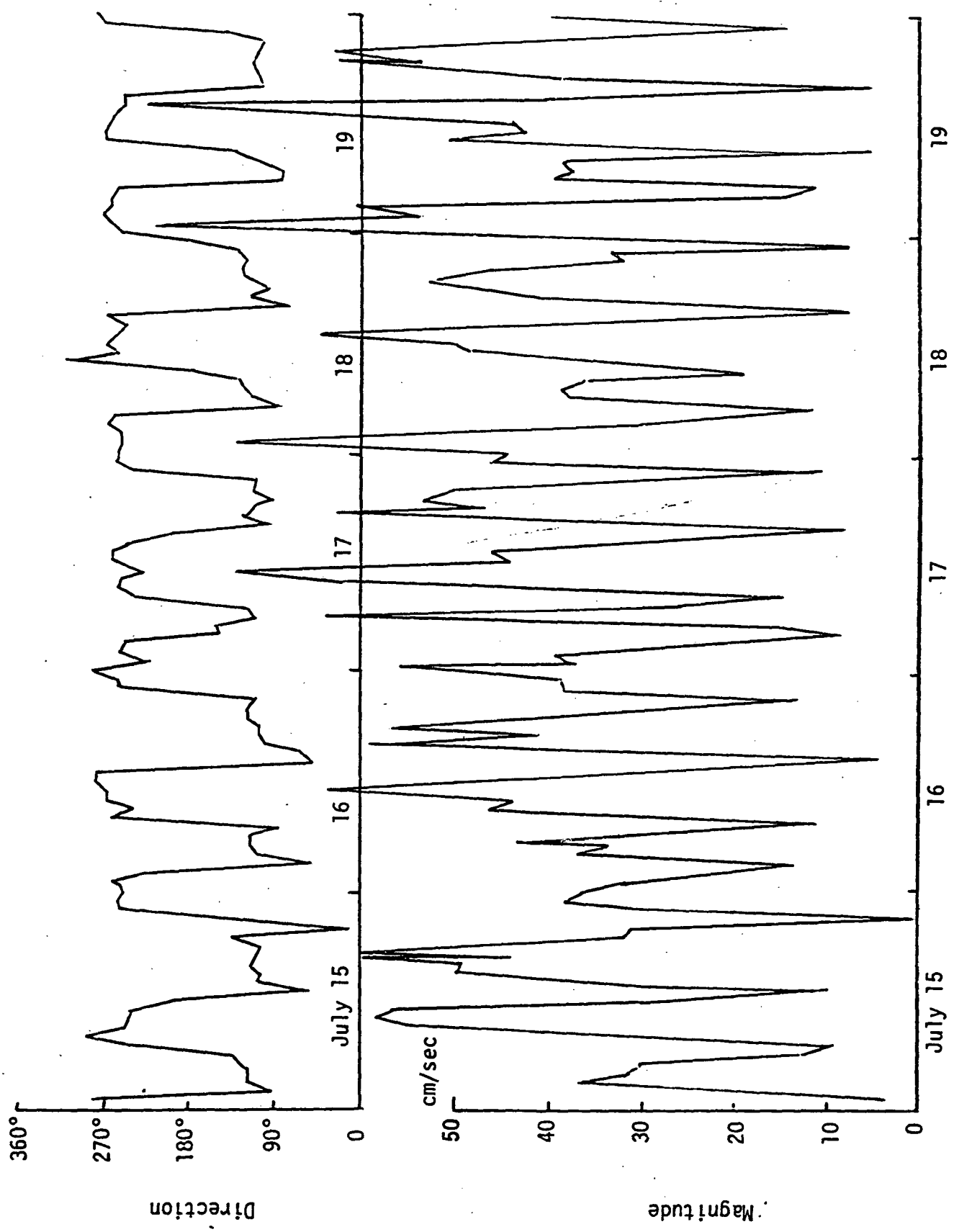

Figure 3.8. Current meter data at Mark 13 on Figure 3.3

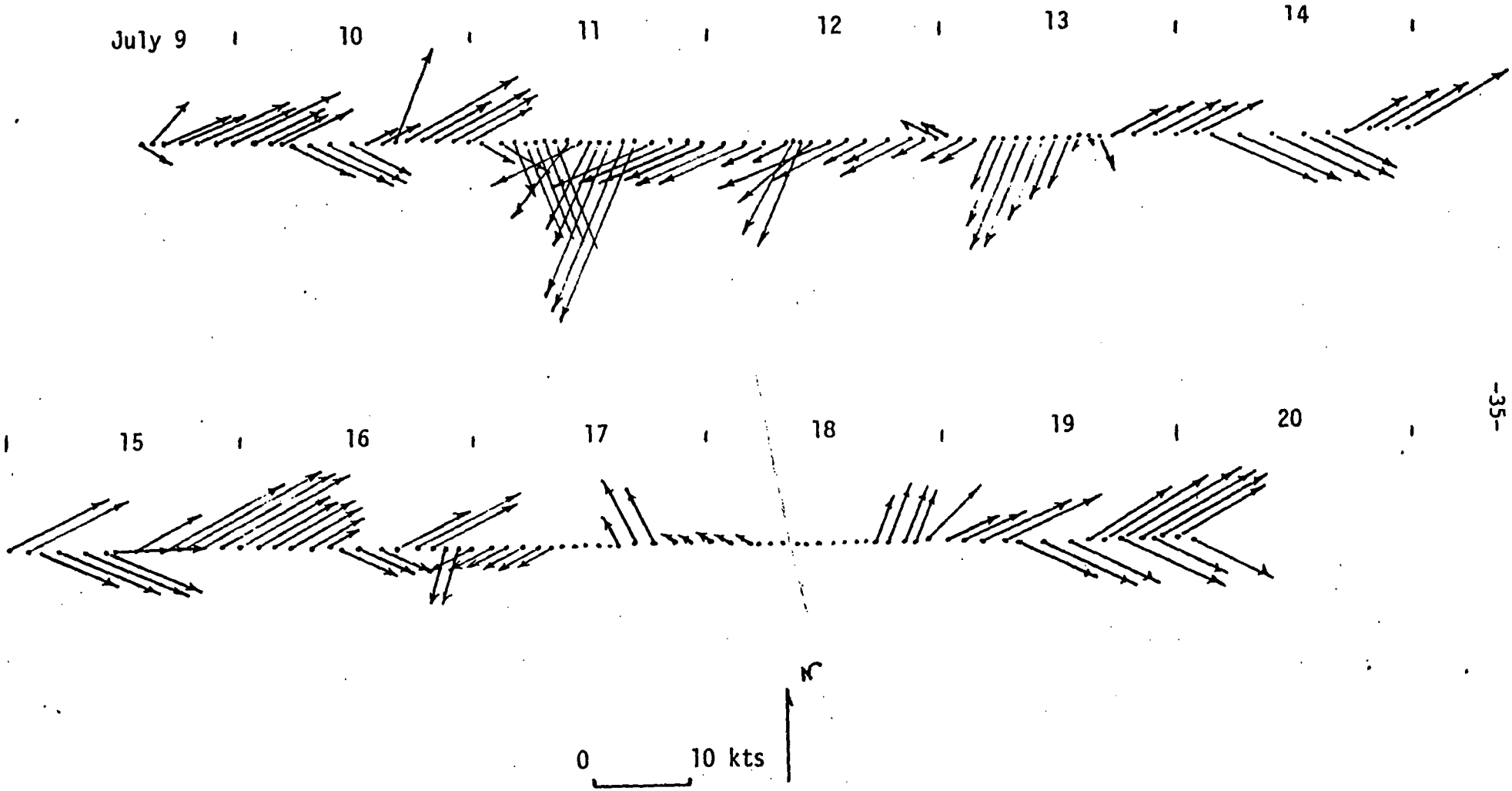

Figure 3.9. Wind data at station shown on Figure 3.3

flight was chosen to be coincident with one of the days when inlet current measurements were being made at one of the inlets by the ground crew using floating buoys dropped from a small boat and tracked by two surveyor transits on an island in the mouth of the inlet.

It was hoped that sequential photographs taken from the aircraft as it passed over the inlet could be used as a means of measuring buoy positions and velocities in order to provide an independent check on the transit measurements. It turned out, unfortunately, that the aircraft altitude required to enable observation of sufficient land mass to permit measurement of relative location of buoys with respect to land was so high that the small buoys used (approximately 2 foot cubes) could not be seen in the photographs.

Initial planning envisioned two data acquisiton flights on each of two days: one flight each day at ebb tide and one at flood tide, and one day for Hatteras Inlet and one for Ocracoke Inlet. The days initially chosen as most desirable based on North Carolina State University research project schedules and time of occurence of ebb and flood tides were: 10 July at Hatteras and 15 July at Ocracoke.

Data acquisition runs at an altitude of 500 feet (for best laser operation conditions) were planned to be flown on courses along radials from the center of each inlet mouth; each run to be nominally 10 miles long to ensure that data would be obtained on ocean surface unaffected by inlet currents as well as on ocean surface near the inlet where inlet current effects could be observed.

Also, initial planning called for measurements to be made (simultaneous with the laser measurements) on ocean surface conditions using the NRL nanosecond radar; it turned out that the radar was not available and it was not used.

Although a detailed flight test plan originally had been drawn up for this experiment, it was later modified as will be discussed, to be consistent with final planning practicalities.

Figure 3.10 shows the ground traces of the flight test runs planned for Hatteras Inlet. It can be seen that one run was planned to be flown perpendicular to the beach rather than the inlet. The purpose of this run

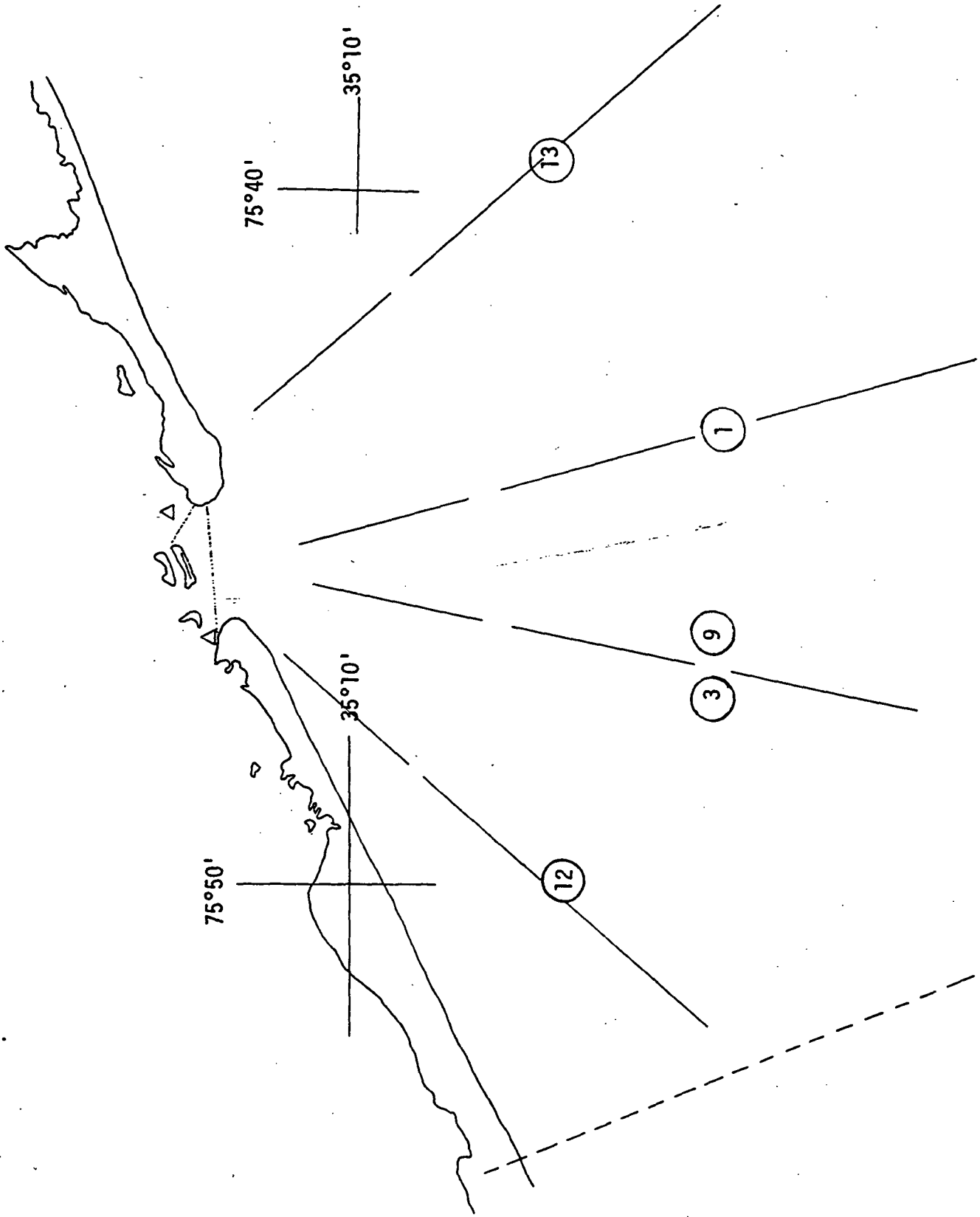

Figure 3.10. Ground Tracks for aircraft measurements.
Numbers in circles indicate the test run numbers.

was to obtain information on changes in surface conditions to be expected due to waves moving in to land unaffected by currents, so that this effect could be accounted for in reducing the data from inlet runs.

The laser profilometer to be flown was a continuous wave type with an integration time of twenty (20) milliseconds. At an aircraft ground speed of 140 knots, this is a minimum spatial resolution of 4.7 ft.

In order to produce reasonable measurements, a wave should be sampled about four times per wavelength, minimum; thus the minimum wavelength observable reliably with the profilometer was about 19 feet. This was judged to be more than adequate, since minimum wavelengths expected were of the order of 60 feet

A. 15 July Flight

The first experimental flight test was conducted on 15 July, 1974. Although the flight test plan called for measurements to be made at Ocracoke Inlet, a pre-flight check with personnel at Hatteras/Ocracoke revealed that ground measurements of current velocity and direction were not possible at Ocracoke due to inability to emplace transits for tracking buoys. Plans to fly data acquisition runs at Ocracoke were, therefore, abandoned.

At this time, the requirement for color photographs of inlet geometry was upgraded to mandatory because field personnel at Hatteras reported that inlet geography differed greatly from that shown on charts used in experiment planning.

On the 15th, it had been previously estimated that ebb tide would peak at 10:00. It was planned that flights should be made near that time to maximize the probability of good data acquisition. Because the aircraft was not able to depart Wallops until almost 8:30 it was necessary to change the sequence of experiments from that in the test plan and begin measurement runs immediately upon arrival at Hatteras. The photographic runs planned for initial activity were postponed until after completion of laser data runs.

The aircraft arrived at Hatteras at 9:30 and the first data run was started at 9:30, after deciding that the plan to conduct runs symmetrically located about the wind direction would have to

be abandoned because the wind direction was observed to be almost parallel to the beach front. This caused wind-wave/current interactions to become inseparable from bottom effects on waves.

Swell was observed to be moving in from about the right direction and it was hoped that the laser would be able to measure interaction between current flowing from the inlet and swell waves. Although the wave patterns in the vicinity of the inlet were observed to be very complex due to interactions between wind-waves, swell waves, inlet current and inlet bottom caused effects, it was decided to go ahead with measurement runs in the hope that inlet current/swell wave interaction effects would be observable far enough from the inlet mouth to escape the complications introduced by wind-wave/inlet bottom effects.

The direction of the first run was chosen to be parallel to the axis of the inlet channel. This run was flown at an altitude of 700 feet and ground speed of 146 knots. The ground track heading was about 162° and the run was flown about 4 minutes, which is about 9.6 nautical miles. The second run was simply an inbound repeat of the first run. Subsequent runs were made displaced 30°, then 60° clockwise from the first two runs, as is shown in Figure 3.10.

By the time the in-bound/out-bound set at 60° CW (runs 5 and 6) were complete, the time was 10:20 a.m. It was then decided that instead of proceeding with the plan to make runs CCW with respect to run #1, it would be better to repeat the CW runs since wind direction was on that side and repetition of data acquisition attempts needed to be conducted while current conditions were still good.

This was done, with completion of the repeat of the 60° CW run set (runs 11 and 12) at 11:05. At this time, runs 13 and 14 were flown 30°CCW from run #1, at a ground track heading of approximately 134° (and 314°).

Following the completion of this one CCW set of runs, the planned runs out from and into the beach at a point some 5 to 7

Table 1. July 15, 1974, Flight Pattern Data

Run No.	Time Start	Time End	Begin Lat. & Long.	End Lat. & Long.
1	9:34:35	9:38:37	35°10.8'N 75°45.8'W	35° 1.3'N 75°41.8'W
2	9:41:40	9:46:00	34°59.8'N 75°40.9'W	35°11.6'N 75°45.8'W
3	9:49:00	9:53:07	35°11.6'N 75°45.4'W	35° 2.6'N 75°48.6'W
4	9:57:05	10:01:08	35° 1.3'N 75°49.3'W	35°11.8'N 75°46.2'W
5	10:03:37	10:08:37	35°11.8'N 75°46.2'W	35° 8.9'N 75°54.5'W
6	10:12:11	10:16:45	35° 2.0'N 75°55.9'W	35°12.0'N 75°46.6'W
7	10:19:30	10:23:35	35°12.2'N 75°45.7'W	35° 2.8'N 75°42.2'W
8	10:27:40	10:32:30	35° 0.8'N 75°41.3'W	35°12.3'N 75°45.6'W
9	10:35:43	10:40:11	35°12.5'N 75°45.2'W	35° 2.6'N 75°48.0'W
10	10:44:20	10:48:28	35° 1.6'N 75°47.8'W	35°12.5'N 75°45.2'W
11	10:51:30	10:56:05	35°12.7'N 75°45.1'W	35° 4.6'N 75°53.0'W
12	11:00:00	11:04:00	35° 3.8'N 75°52.9W	35°12.7'N 75°45.4'W
13	11:06:35	11:10:57	35°12.7'N 75°45.0'W	35° 4.9'N 75°35.5'W
14	11:14:55	11:20:37	35°03.2'N 75°33.9'W	35°13.0'N 75°45.4'W
15	11:24:15	11:29:09	35°10.8'N 75°51.1'W	35° 1.8'N 75°41.1'W
16	11:34:56	11:39:00	35° 0.1'N 75°49.6'W	35° 9.3'N 75°54.7'W

miles SW of Hatteras Inlet along Ocracoke Island were flown, again at an altitude of 700 feet. The headings for these were 150° and 330°, approximately. This completed the data acquisition portion of the flight. Table 1 shows the time, heading, ground speed, and corrected end point coordinates for all data runs.

During the portions of some of these runs when the aircraft was in the vicinity of the inlet, photographs were made even at the high altitude involved in the hope that a floating buoy would be observed in relation to a land mass. This did not happen.

After completion of the final data acquisition run, the aircraft proceeded to Ocracoke Inlet where photographs were taken at altitudes of 5,000 and 8,000 feet. Photographs were then taken at Hatteras Inlet at 8,000 feet altitude, with these completed at 12:15 p.m. The aircraft then returned to Wallops Flight Center, arriving at 1:15 p.m.

The film from the aerial photographs was delivered to photo processing and the laser data was taken to NRL to be converted to digital form and processed. The results obtained are discussed in Section 3.4.

B. Flight on 17 and 18 October, 1974

A second group of flights was executed on October 17 and 18, 1974, to obtain data during flood conditions at Ocracoke before the inlet geometry had undergone substantial changes due to winter storms. The same flight plan as that of the July 15, 1974, test was essentially adopted.

However, due to an undetected malfunction of the laser profilometer, no useful data were collected during these flights. Therefore discussions of test results presented in this report will be limited to these data obtained on the flight of July 15, 1974.

3.4 Remote Sensing Results

The July 15th flight data were processed at the Naval Research Laboratory, Washington, D. C. Since the sea state during this flight was low,

a number of data anomalies occurred on each run of the flight; the laser profilometer did not provide continuous data. Therefore the single run data were cut into segments of 28 second duration and only those segments which were free of anomalies were processed.

Five typical runs are selected for this report. The wave spectra for selected 28 second segments of these runs are shown in Figures 3.11 through 3.15. Probability density functions (for the surface height fluctuations) for these same segments are shown in Figures 3.16 through 3.20

From Table 3.1 we see that Run 1 occurred between 0934 and 0939 and Run 3 occurred between 0949 and 0953. During the time period 0934 and 0953 the wind was approximately 12 knots from 120°. These two runs tracked sufficiently similar wind and current conditions to allow an inter comparison on the basis of theory. Runs 9 and 12 occurred when the wind direction and magnitude were changing and might be intercompared but should not be compared with Runs 1 and 3.

Run 1 is the most encouraging in terms of theory valuation. Figure 3.11 shows a pronounced spectral change and increase in energy as one approaches the inlet. In the inlet case, the water coming out of the mouth during ebb tide will diverge and hence decrease in speed. As a result the wave energy should be higher near the inlet and decrease as the distance from the inlet increases. This is the result shown for Run 1 in Figure 3.11. As the energy of the wave field increases, the variance of the distribution of wave heights increases. This is clearly evident for Run 1 in Figure 3.16. However, agreement between theoretical predictions and the observed spectral and density function cannot be made quantitative. At this time it is not possible to locate the geographic wavemakers corresponding to each 28 second data segment. These locations determinations are crucial because of the complex bottom topography and current distributions in the Hatteras Inlet area.

While the data from Run 1 are encouraging, the data from Run 3 are not so easily explained. The first data segment analyzed, occurring farthest from the inlet has a peak value of approximately 2 $ft.^2/Hz$ occurring at .35 Hz. The spectrum for the farthest position in Run 1 had a peak value of less than one $ft.^2/Hz$ occurring at approximately 0.6 Hz. It is likely

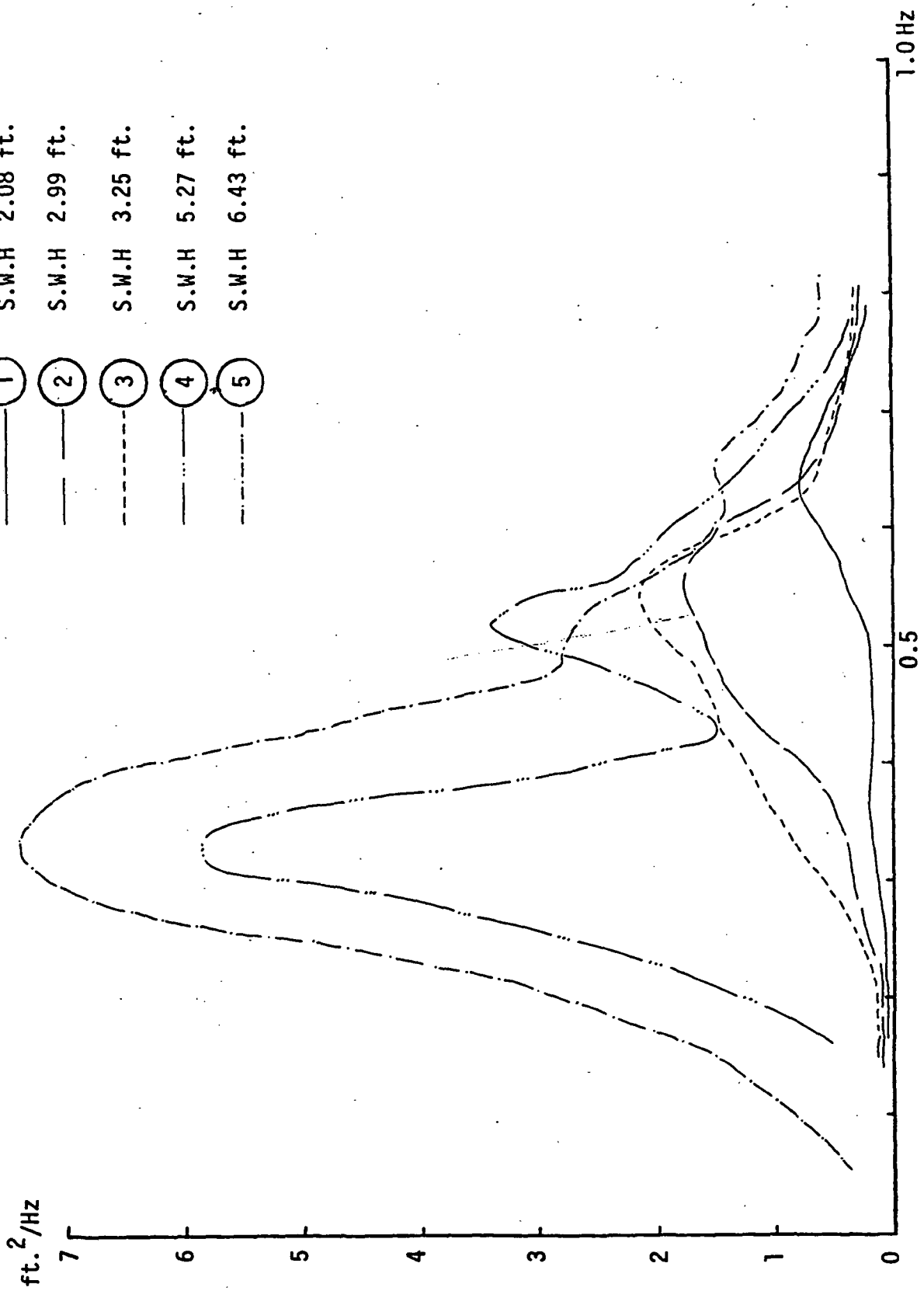

Figure 3.11. Frequency spectra measured by laser profilometer for Run No. 1.
Numbers in circles increase as the distance gets smaller to the inlet.

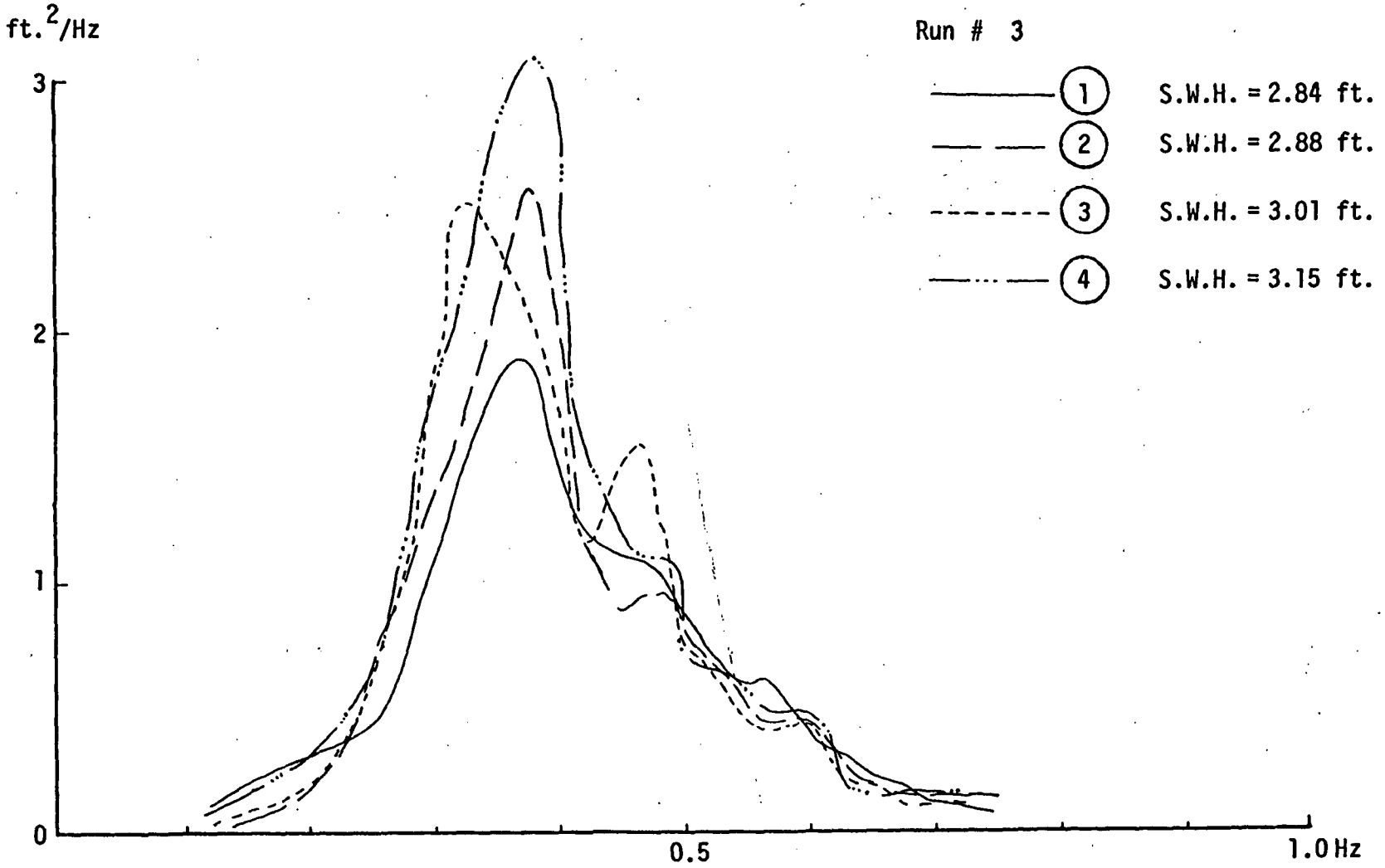

Figure 3.12. Frequency spectra measured by laser profilometer from Run No. 3. Numbers in circles increase as the distance gets smaller to the inlet.

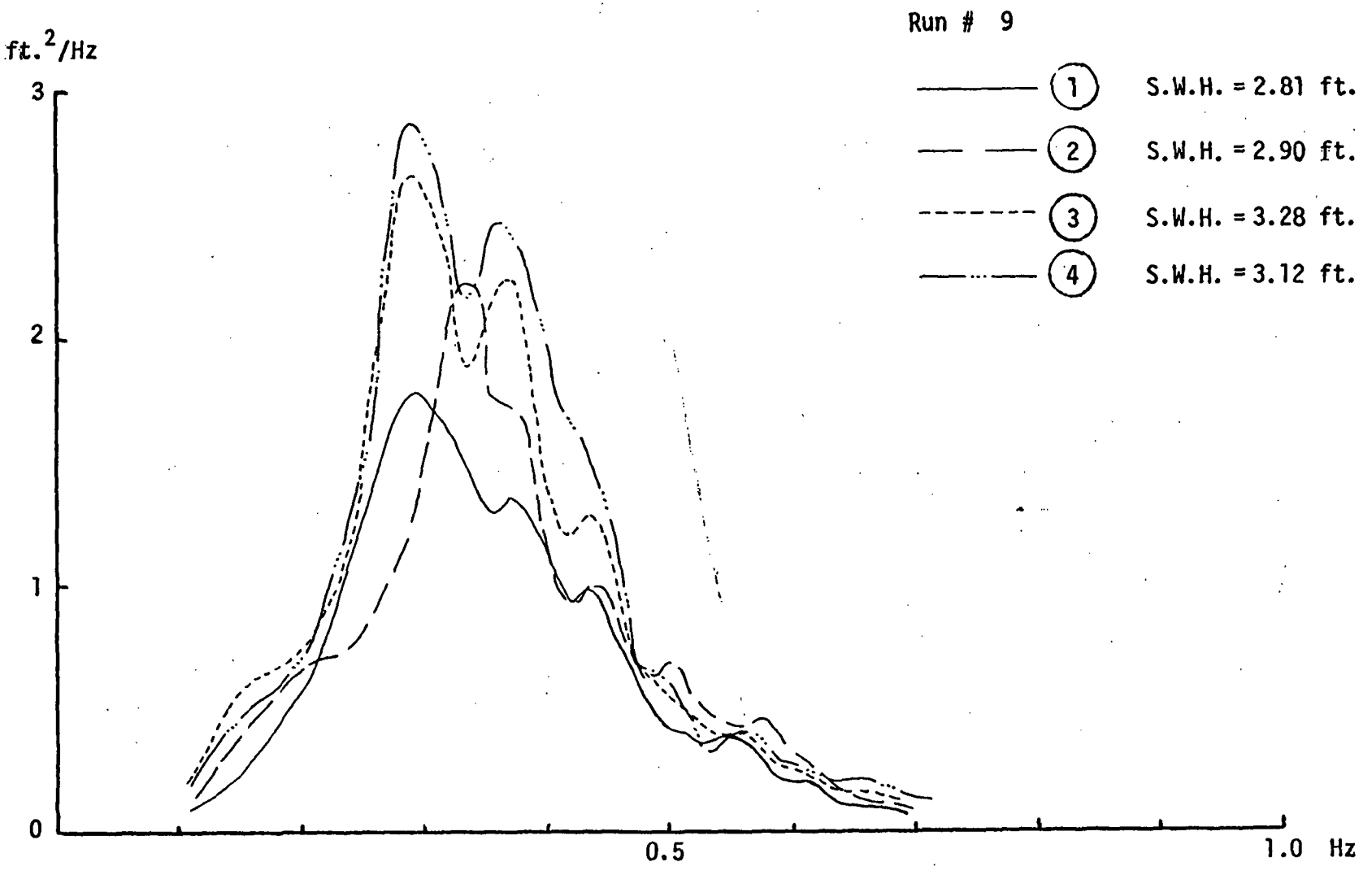

Figure 3.13. Frequency spectra measured by laser profilometer for Run No. 9. Numbers in circles increase as the distance gets smaller to the inlet.

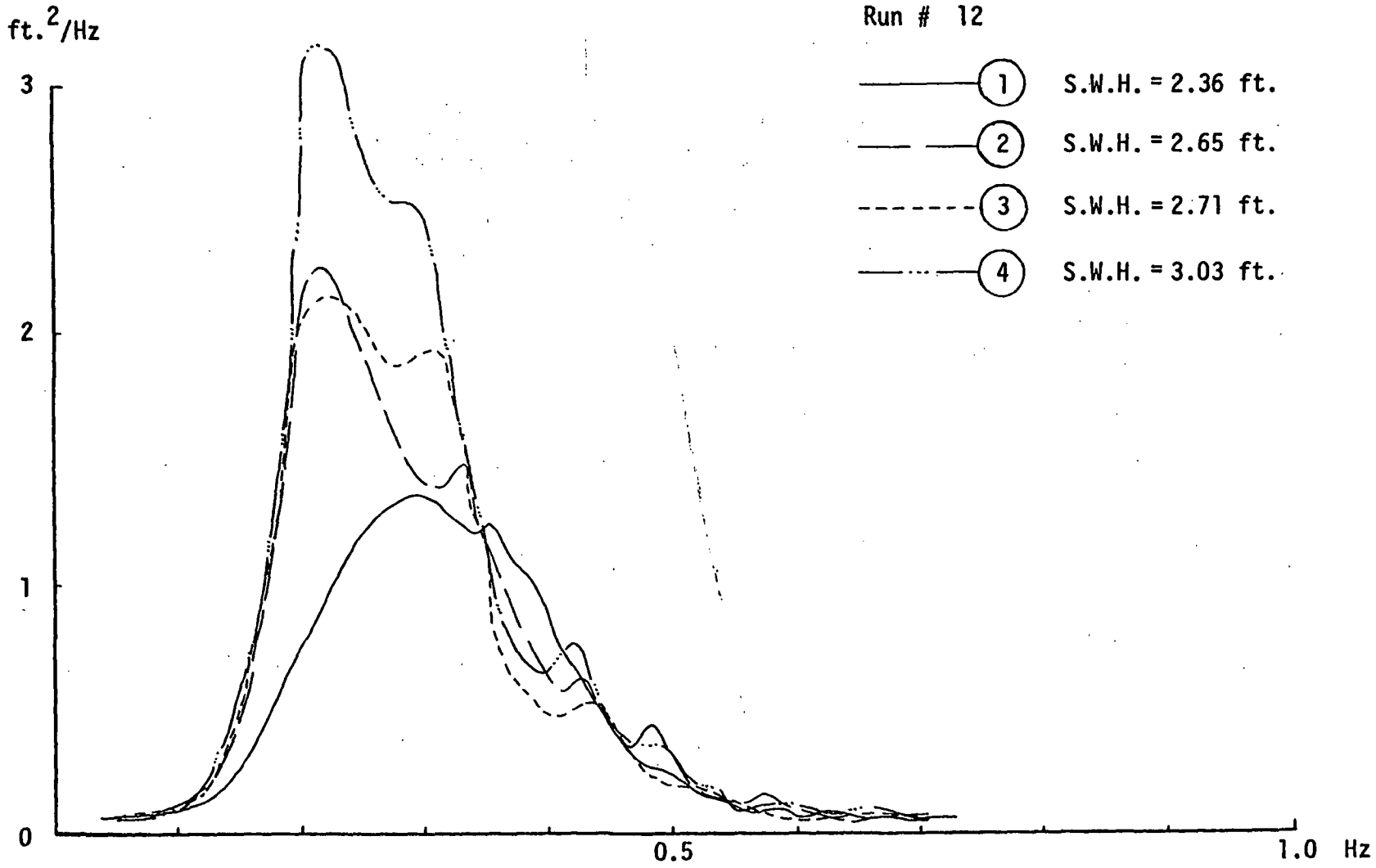

Figure 3.14. Frequency spectra measured by laser profilometer for Run No. 12. Numbers in circles increase as the distance gets smaller to the inlet.

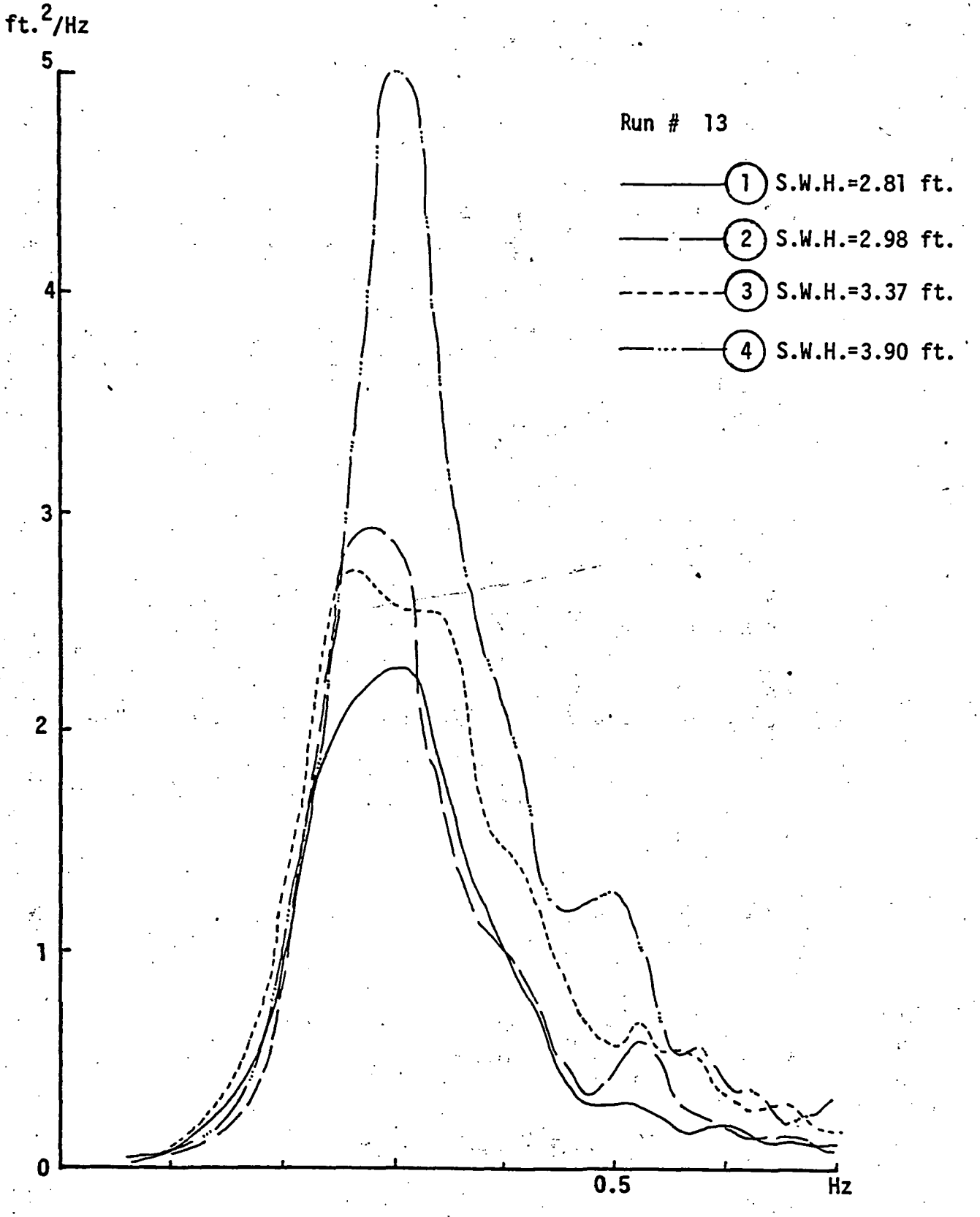

Figure 3.15. Frequency spectra measured by laser profilometer for Run No. 13. Numbers in circles increase as the distance gets smaller to the inlet.

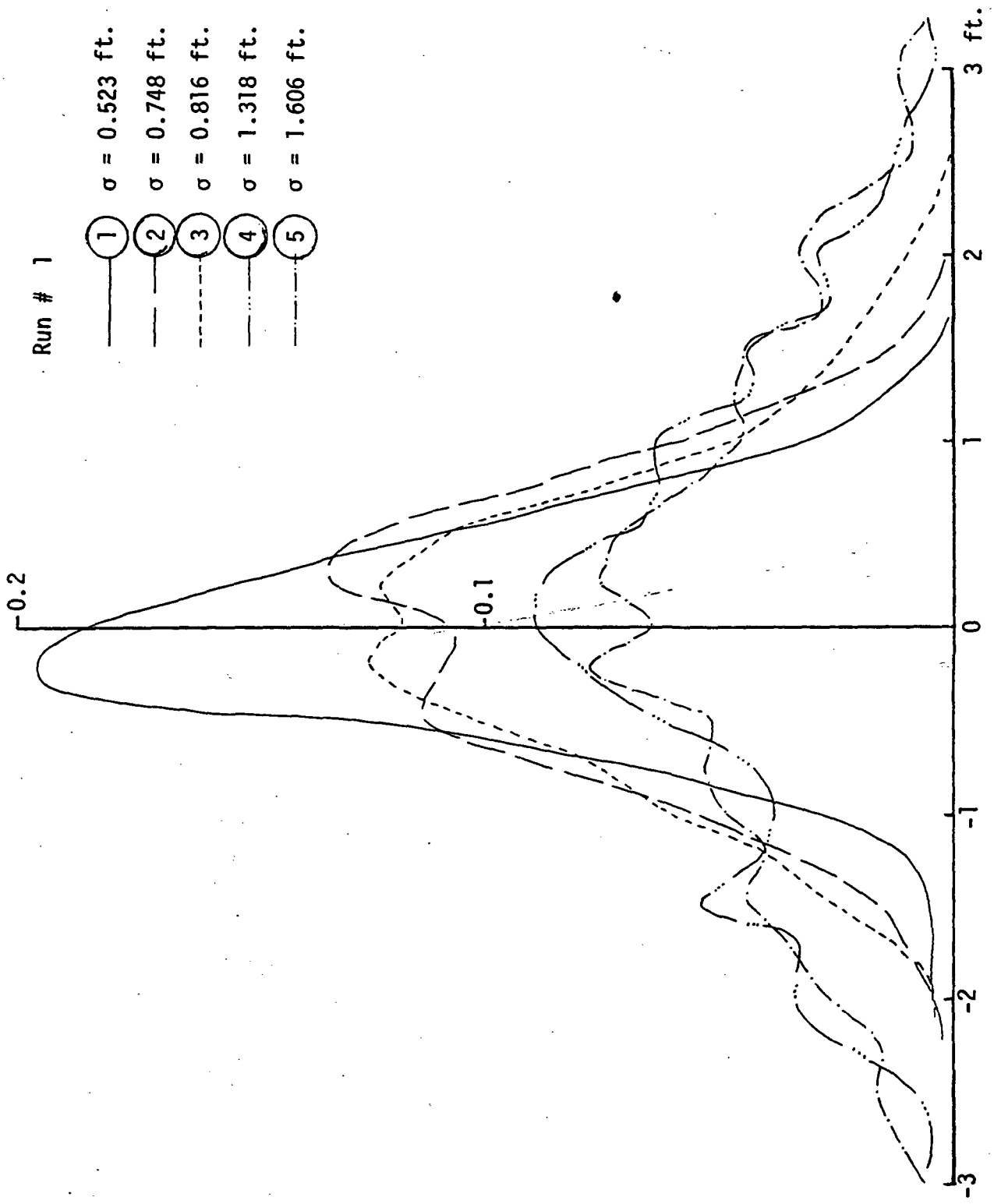

Figure 3.16. Probability density distribution curves for Run No. 1.
Numbers in circles increase as the distance to inlet decreases.

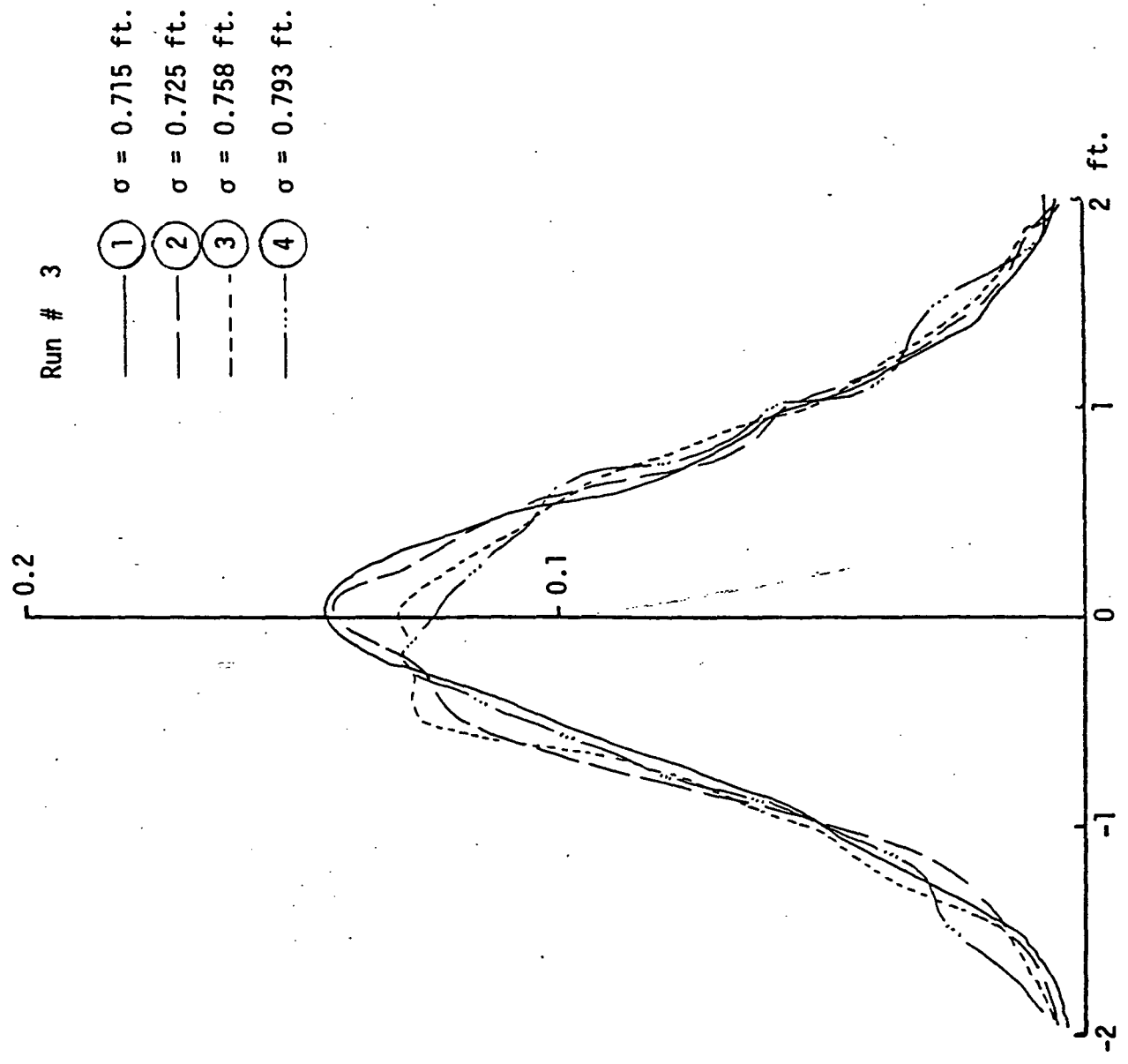

Figure 3.17. Probability density distribution curves for Run No. 3. Numbers in circles increase as the distance to inlet decreases.

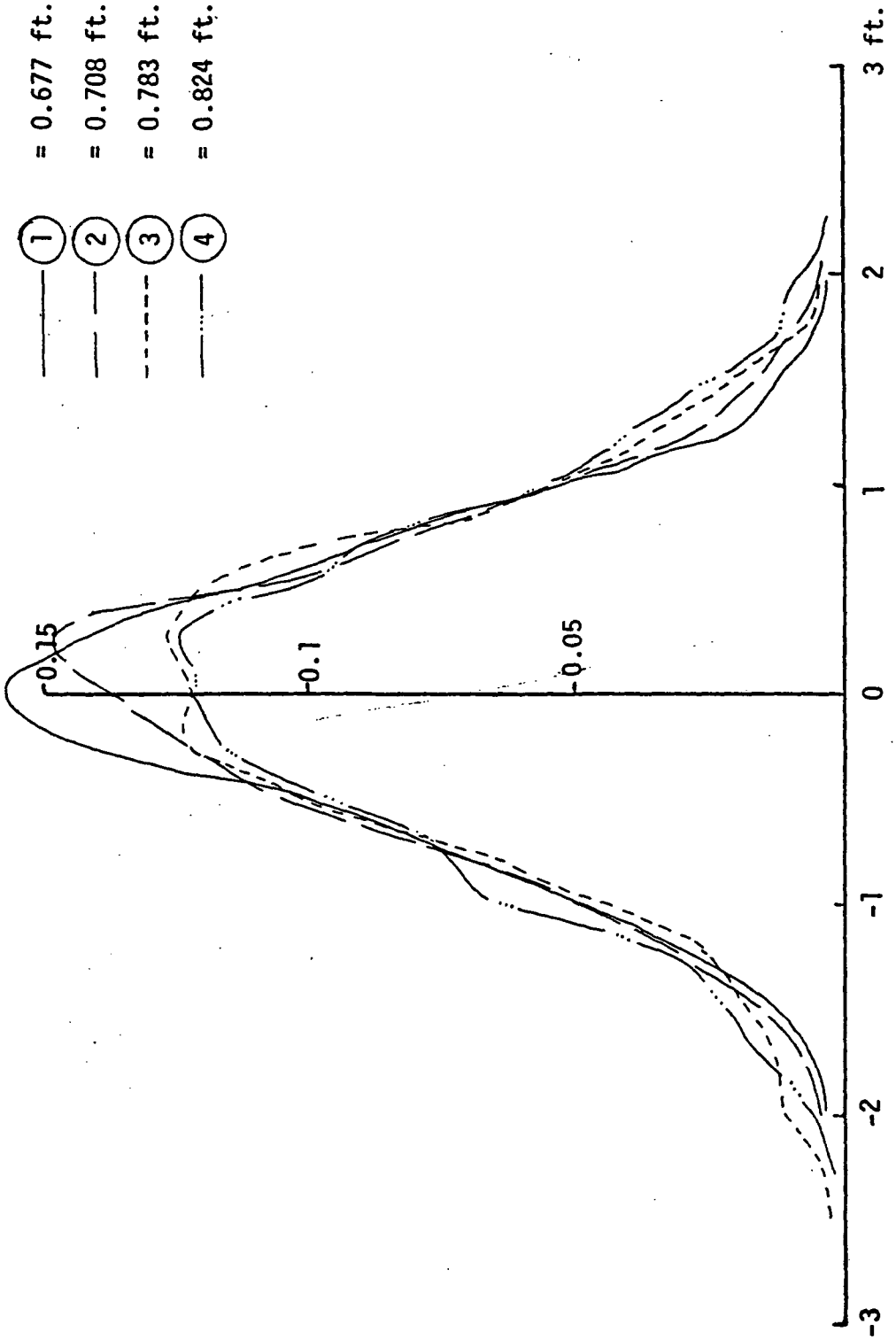

Figure 3.18. Probability density distribution curves for Run No. 9.
Numbers in circles increase as the distance to inlet decreases.

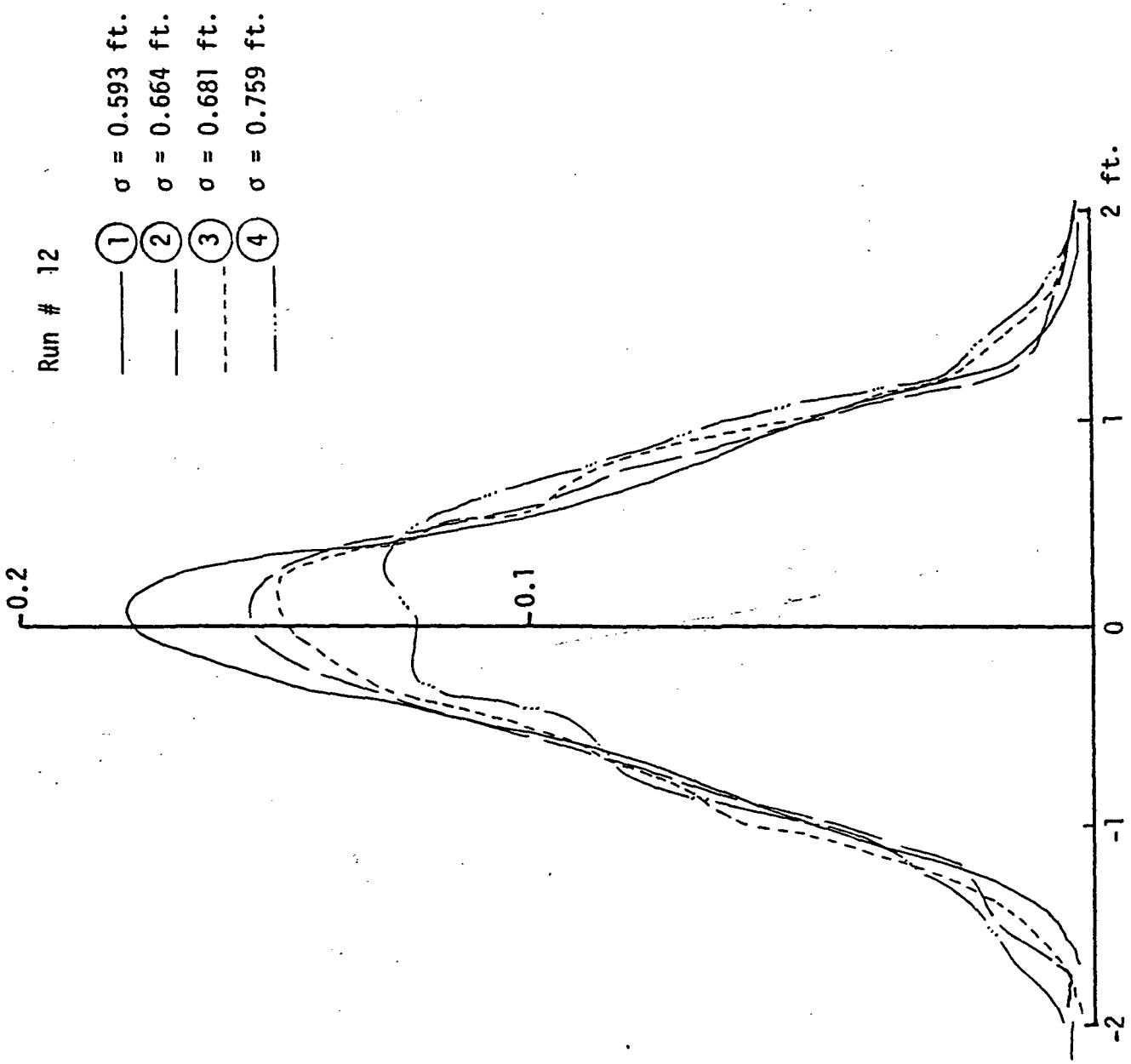

Figure 3.19. Probability density distribution curves for Run No. 12.
Numbers in circles increase as the distance to inlet decreases.

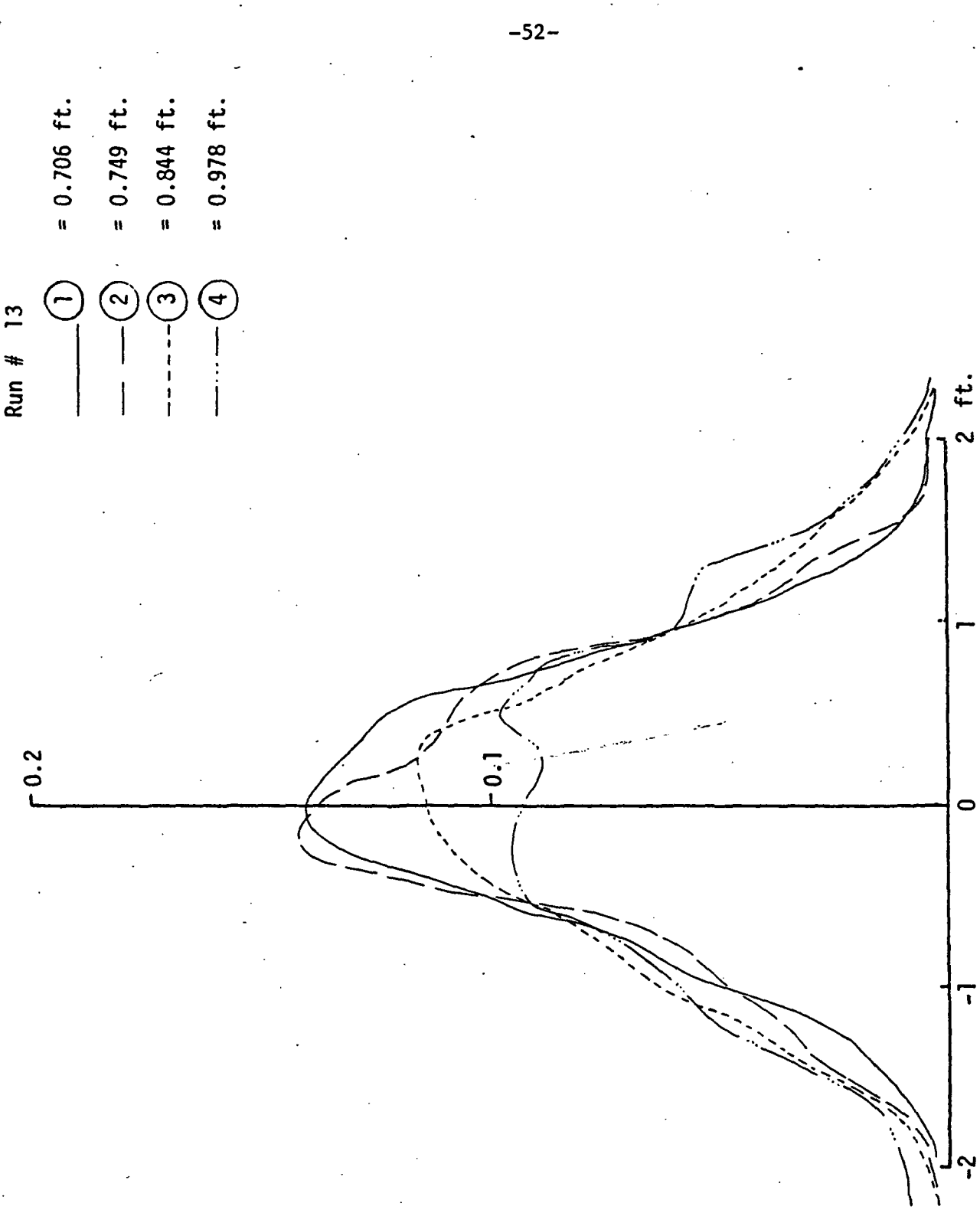

Figure 3.20. Probability density distribution curves for Run No. 13.
Numbers in circles increase as the distance to inlet decreases.

that the first spectrum for Run 1 was taken at a considerably greater distance from the inlet mouth than was the first spectrum of Run 3. Nevertheless as one approaches the inlet the spectra for both runs peak at about .35 hertz although the peak value of Run 1 is almost twice the peak value of Run 3. It may be that this period, $(.35)^{-1}$ seconds, is a consequence of the bottom topography as well as current effects. In view of our inability to locate the positions appropriate to each 28 second data segment and the complex current distribution and bottom topography, it does not seem fruitful to attempt further inter comparisons between Runs 1 and 3.

Notwithstanding these shortcomings, Run 1 will be discussed in more detail to provide evidence of feasibility of the use of wave-current interactions as a means of measuring current. The reasons for picking this set of data are as follows: (1) Run 1 is along the axis of the inlet where the current is strongest and the direction of the current is well defined as indicated by the buoy studies; (2) by the theory of wave-current interactions discussed in Chapter 2, the waves along this path should turn sufficiently so that the wave vector will be almost parallel to the current on the axis of the inlet. If this happened, the flight path will be along the wave vector at least for a short distance; (3) from this Run alone, five 28-second segments were chosen, so that the data from this run were the most dense and complete. Spectra changes along this path are shown in Figure 3.11. The lowest curve represents the sea state farthest from the inlet while the highest represents that nearest to the inlet. A different way to present the spectra is shown in Figure 3.21. The energy spectra indicate the change due to current conditions. The spectral form also roughly indicated saturation in the higher frequency range as predicted by a previous report (Huang, et al. 1972) and Phillips (1966).

The probability density functions in Figure 3.16 show the same trend as discussed in Section 2.3. It should be pointed out that the maximum readings of the probability density function curves are considerably lower than the theoretically predicted values under the given wind and current conditions. This is probably due to the sensitivity of the instrument used. The theoretical curves shown in Figures 2.9 through 2.12 were calculated with a short wavelength cut off value of 1 ft., while the smallest wave that the laser profilometer was capable of measuring was calculated

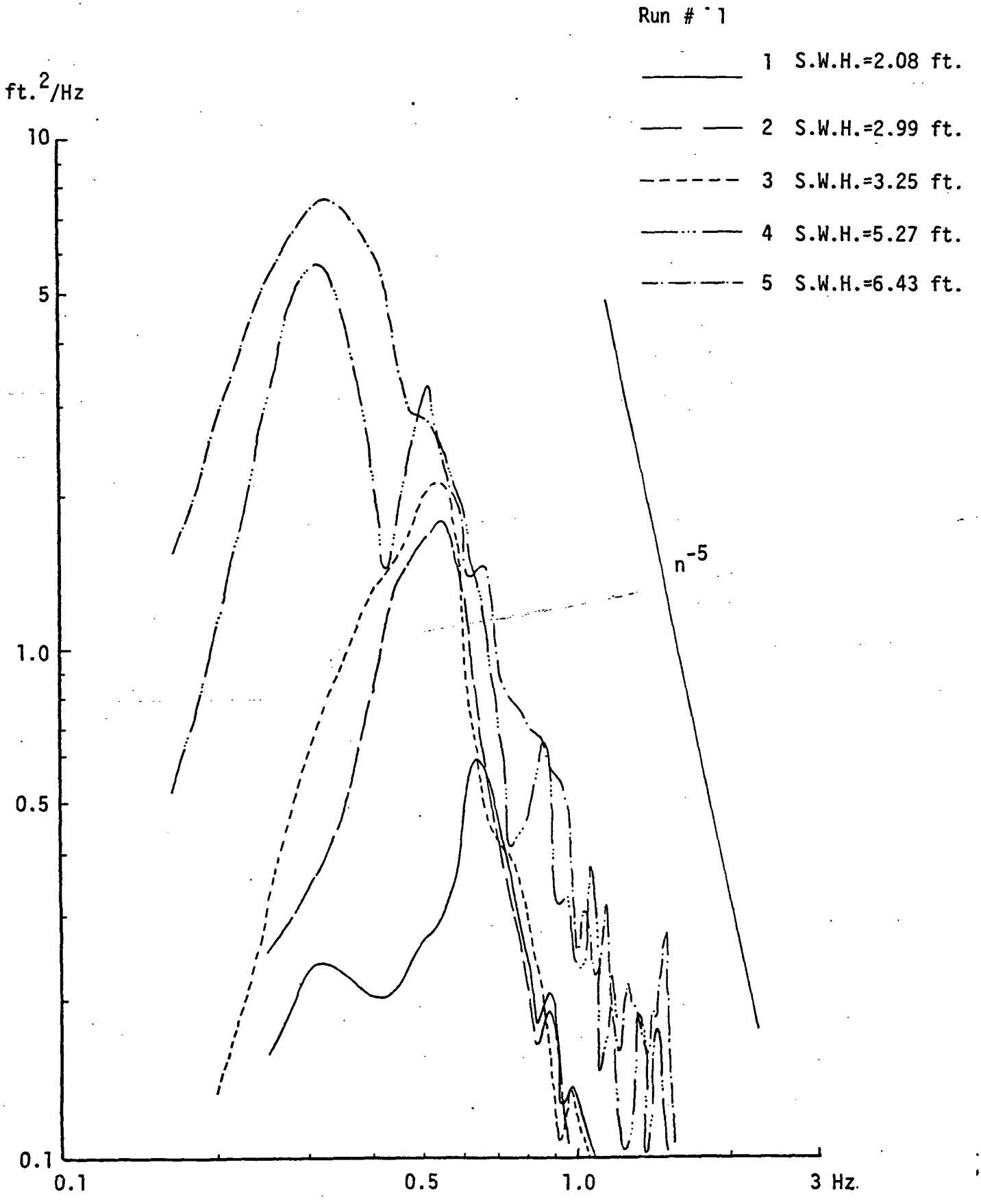

Figure 3.21. Frequency spectra of Run No. 1 on log scale.

in the previous section to be around 20 ft. in length. This difference is substantial, but the discrepency was expected.

The trend of the events observed, however, is extremely encouraging. The technique of the use of wave-current interaction as a means of making current measurements has also received independent support from a study by Parson (1974). In that study AGC samples from the SKYLAB S-193 altimeter were processed. Strong correlations between the signal strength and the locations of the major current system were found.

Additional studies are needed to investigate and validate both these methods and to establish the quantitative relationships needed for operational use of either.

4.0 CONCLUSIONS AND RECOMMENDATIONS

4.1 Conclusion

From this study, it has been established qualitatively that wave-current interactions can be used to detect currents at the regions where strong current gradients exist. This method offers an alternative remote sensing method of detecting ocean current, which differs from those used previously in scatterometery, altimetry, laser wave profiling and air-borne short-pulse radar, but which can be applied to data collected by one or all of these. The experiments conducted during the period of this study were not intensive enough to establish the required quantitative relationships. Furthermore, only one of the above mentioned instruments was used. Though the principle of using wave-current interactions has been established to a certain extent in theory and in laboratory experiments, the technique is still not fully developed and has not yet been completely proven. Considerably more data are required to establish the quantitative relationships needed to be able to use this method of current detection operationally. The results from the present study offer a start in this direction, and have proven to be invaluable as a precursor to improved future efforts.

4.2 Recommendation

A number of shortcomings became obvious during this study. The following suggestions are made to help in avoiding some of them in future studies.

A. Add time scale in data recordings.

In the laser recording system, a time scale will have to be build in so that the exact geographic location of the data points can be established. This is crucial especially in the strong current gradient cases where a small error in locations can change the associated current value substantially. The development of quantitative relationships will require exact current values as a crucial input.

B. Incorporate flight directions relative to wave vector other than parallel in the laser data reduction program.

The present laser data reduction program is written based on the assumption that waves and wind are always propagating in the same direction; i.e. the sea is assumed to be a one-dimensional random surface. This assumption is obviously not true as discussed by Phillips (1966). Even if the one-dimensional sea state is accepted as an approximation, the flight angle relative to the wave vector still have to be considered in data reduction. Also, the platform on which the laser profilometer is mounted is moving. This motion should also be considered. Probably a scanning laser surface contour profilometer should be used instead of the present single axis profiler.

C. Additional calculations of the probability density function, with cut off wave length compatible with that of the laser profilometer.

The present theoretical curves are generated by using a short wavelength cutoff of 1 ft. in length, but the laser profilometer can only measure waves longer than 20 ft. New curves have to be generated, especially if a scanning laser profilometer will be used. In the scanning mode, the laser spot will move much faster and the sensitivity will decrease accordingly. The discrepancy with the present theoretical results may thus become even larger.

D. More field experiments.

The whole concept of using wave-current-interaction as a

means of current detection is new. It needs considerably more measurements for verification, with various instruments such as scatterometer, radiometer, altimeter, air-borne laser profilometer and nanosecond radar. Each of the instruments will measure the same phenomenon with a different emphasis. With data from all these, a complete picture can be constructed. Different instruments will also offer a cross check of the results so that a definitive quantitative relationship can be established with confidence for operational use.

Part II - Remote Sensing of Ocean Currents by Backscattering Cross Section Measurements

1.0 INTRODUCTION

In Part I of this report, it was theoretically and experimentally demonstrated that currents affect a change in the probability density function of the height of the surface waves. This alteration arose because of a change in the mean-square height of the waves. Since the probability density function of the wave elevation has a direct effect on the average return waveform detected by a downward-looking short pulse radar, such an instrument can be used to determine the presence and, conceivably, the magnitude of currents. However, in order to evaluate the sensitivity of the waveform technique relative to ocean current sensing, it would be necessary to carry out a very detailed study of the trade-offs between transmitted pulse width, pulse repetition frequency, averaging time and surface roughness homogenity similar to that conducted by Miller and Brown (1974). While such a study is definitely essential to future work on remote sensing of currents, it was felt to be beyond the scope of the present effort.

Large scale ocean currents are, in addition, known to alter the local geoidal height and also influence the backscattering cross section of the ocean surface. Since the effects of currents on geoidal height are presently being studied elsewhere, it was decided to direct this study toward quantizing the influence of currents on the surface backscattering cross section or σ°. Of all the consequences of ocean currents previously mentioned, the measurement of σ° is probably the easiest to accomplish. However, it is the purpose of this material to determine whether the influence of currents on σ° is truly detectable or merely a second order effect.

The basis for this effort is formed by the work of Huang, et al. (1972) in which the effects of ocean currents on the one-dimensional wave height spectrum and the mean squared slope were determined. In this report, we use these results to calculate the effect of currents on σ° for both large angles of incidence and normal incidence and to determine the feasibility of using such a measurement as a current sensor.

Before continuing, however, it should be pointed out that the theory developed by Huang, et al. (1972) is applicable only to the so-called "gravity

wave" range of the wave height spectrum. Furthermore, there is no justification for attempting to extend this theory into the capillary range of the spectrum. This limitation will impose some rather severe restrictions upon our analysis of the effects of currents on σ°; however, until the effects of current on the capillary range are more completely known, these restrictions must be understood and tolerated.

2.0 THE EFFECT OF CURRENTS UPON σ° FOR LARGE ANGLES OF INCIDENCE

For large angles of incidence ($\theta \geq 45^\circ$), the backscattering cross section is determined by those surface waves which satisfy the Bragg condition, i.e.

$$\lambda_{rf} = \frac{4\pi}{k} \sin\theta \quad , \tag{2.1}$$

where λ_{rf} is the wavelength of the radar, θ is the angle of incidence and k is the wavenumber of the ocean wave. Because of antenna aperture limitations and resolution requirements, it is desirable to "select" a value of k which yields a minimum radar wavelength. Quite obviously from equation (2.1) this can be accomplished if k is maximized.

If k is to be made large, then this implies that the radar wavelength will be in resonance with a ocean wavenumber in the so-called equilibrium range of the surface height spectrum. Using Huang's results for the effect of current on the spectrum in the equilibrium range, we find that the ratio of σ° including current to σ° for no current is given by

$$\frac{\sigma^\circ(U)}{\sigma^\circ(U=0)} = \left\{ 1 + \frac{2U\sqrt{k/g}}{1 + \left[1+4U\sqrt{k/g}\right]^{1/2}} \right\}^{-7} \tag{2.2}$$

where $g = 9.8$ m/sec^2. In order to maximize the sensitivity of $\sigma^\circ(U)/\sigma^\circ(U=0)$ to changes in U, we note by inspection of equation (2.2) that this can be done by "selecting" the maximum value of k. Hence, both the requirement to minimize λ_{rf} and to maximize the sensitivity of $\sigma^\circ(U)/\sigma^\circ(U=0)$ are satisfied by "selecting the largest possible value of k.

Unfortunately, we are not at liberty to arbitrarily "select" k since there are two other conditions which must be satisfied. These conditions are imposed by; (1) the spectral isotropy assumption implicit in equation (2.2); and (2) the requirement that we not exceed the spectral range for which gravity waves are dominant (a condition imposed by the linitation of Huang's analysis to the gravity wave region).

In equation (2.2), we have assumed that we are dealing with ocean wavenumbers for which the waves spread isotropically. This assumption was made for two reasons; the first of which is that our knowledge of the directional characteristics of the spectrum is rather poor and, thus, that part of the spectrum which is not isotropic should be avoided. A second reason is that in order to sense ocean currents, a flight path perpendicular to the current would be chosen so that as the craft crossed the current boundary a rapid change in radar cross section would define the position of the current interface. For this geometry, we would want to observe (with the radar) those waves which can propagate at large angles from the wind direction; in other words we must restrict our attention to isotropic waves. Based on an analysis of the results of measurements by Longuet-Higgins, et al. (1963), Miller, et al. (1972) have concluded that isotropic waves are (conservatively) defined by the following:

$$0.03\ w\sqrt{k} \geq 1 \tag{2.3}$$

where w is the wind speed in meters/sec and k is the wavenumber in 1/meters. Equation (2.3) defines the condition imposed by the isotropy assumption.

As noted previously, Huang's theory on current-wave interaction is only valid in the gravity wave region of the spectrum. Based on Cox and Munk's (1954a) measurements of oil slick damped waves, Huang, et al. (1972) have concluded that a cutoff wavenumber equal to 20.9 m^{-1} ($\lambda_c = 0.3m$) is a reasonable upper bound on the validity of their analysis. Thus, we must satisfy

$$k \leq 20.9\ m^{-1} \tag{2.4}$$

With 20.9 m^{-1} as the maximum permissible value of k, we determine that the results of this analysis are valid provided $w \geq 7.3$ m/sec (equation (2.3)). Furthermore, we see from equation (2.1) that the radar wavelength and angle of incidence are pair-wise uniquely determined; permissible values of angle of incidence and radar operating frequency are given in Table I.

TABLE I

Pairwise values of angle of incidence and frequency which satisfy the Bragg condition for k = 20.9 m^{-1}.

θ (degrees)	f_{rf} (MHz)
45	706
50	651
55	609
60	576

Using k = 20.9 m^{-1} in equation (2.2) will yield the maximum sensitivity of $\sigma^\circ(U)/\sigma^\circ(U=0)$ to current since 20.9 m^{-1} is the maximum permissible value of k. A plot of the dependence of $\sigma^\circ(U)/\sigma^\circ(U=0)$ upon current is shown in Figure 2.1. When U is positive, the wind and current directions are parallel; when U is negative, the wind and current directions are anti-parallel. For $U < -0.2$, the surface waves are evanescent and the analysis is no longer valid since the waves do not propagate.

An inspection of Figure 2.1 clearly indicates that the large angle of incidence backscattering cross-section is a very sensitive function of current speed and direction. Furthermore, we note that the relationship between current and cross section is independent of wind speed (a consequence of the equilibrium spectrum) and is strictly monotonic. Thus, a measurement of σ° should result in a nonambiguous measure of the current. In theory, at least, this analysis indicates that the Bragg scatter geometry is a very suitable configuration for detecting current changes.

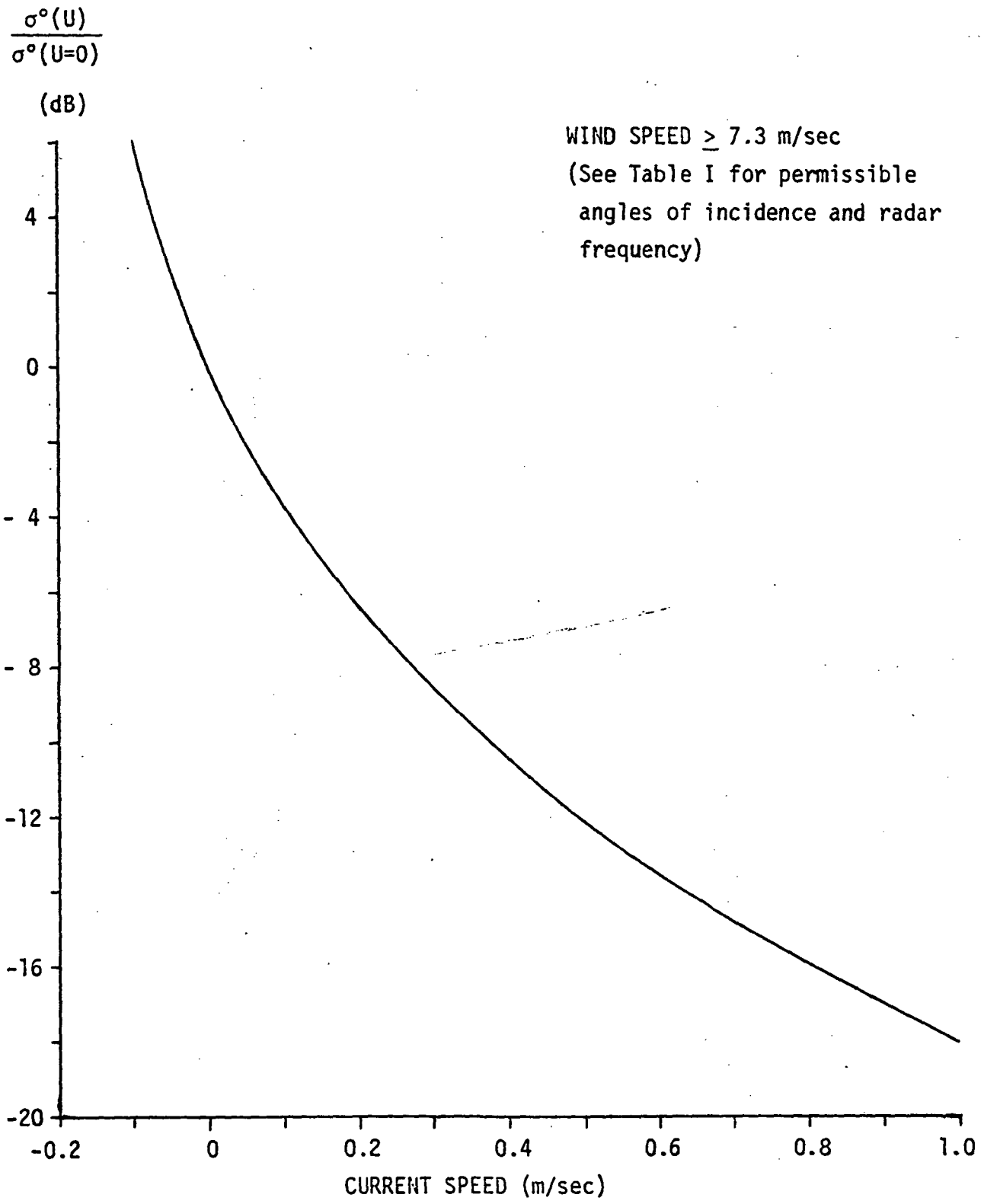

Figure 2.1. Dependence of wide angle of incidence backscattering cross-section upon current.

From a practical standpoint, there is some question as to the suitability of the relatively low radar frequency to aircraft operation. Furthermore, the 18 dB decrease in σ° for a parallel 1 m/sec current would surely require a very sensitive receiver since the resultant signal-to-noise ratio may be less than 0 dB.

3.0 THE EFFECT OF CURRENTS UPON σ° AT NORMAL INCIDENCE

For normal incidence ($\theta=0$), the backscattering cross section of the ocean surface is related to the wave height spatial autocorrelation function $\rho_n(r)$ through the following equation;

$$\sigma^\circ = \frac{8\pi^2 |R_o|^2}{\lambda_{rf}^2} \int_o^\infty e^{-16\pi^2 (h_m/\lambda_{rf})^2 [1-\rho_n(r)]} \, r \, dr \qquad (3.1)$$

where R_o is the Fresnel reflection coefficient at $\theta = 0^\circ$ and h_m^2 is the mean squared height of the waves. Under the assumption that $\rho_n(r)$ is analytic at $r = 0$ and that the integrand decays very rapidly as r departs from zero, we can expand $\rho_n(r)$ in a two-term power series about $r = 0$, i.e.

$$\rho_n(r) \approx \rho_n(0) + \frac{1}{2} \frac{\partial^2 \rho_n(r)}{\partial r^2}\bigg|_{r=0} r^2 \quad . \qquad (3.2)$$

Substituting (3.2) in (3.1) and noting that the mean squared slope is defined by

$$s_m^2 = -2 h_m^2 \frac{\partial^2 \rho_n(r)}{\partial r^2}\bigg|_{r=0} \quad , \qquad (3.3)$$

we find that the approximate value of σ° for $\theta = 0^\circ$ is given as follows;

$$\sigma^\circ(\theta=0^\circ) \simeq \frac{|R_o|^2}{s_m^2} \tag{3.4}$$

For ocean surface backscattering applications, there is an inherent problem with equation (3.4). This problem is due to the fact that the mean squared slope is dominated by the high wavenumber portion of the waveheight spectrum (about which very little is known). In fact, if we assume that the spectrum has the Phillips behavior, i.e. $\psi(k) \sim k^{-4}$ for k large, then the mean squared slope becomes infinite as $k \to \infty$. For this reason, it is necessary to introduce the concept of cutoff wavenumber beyond which the spectrum decays much more rapidly than k^{-4}. However, for an asymptotic k^{-4} spectral behavior, the mean squared slope is a very sensitive function of the cutoff wavenumber.

In view of equation (3.4), it would appear that if s_m^2 is sensitive to the cuttoff wavenumber (k_c) then σ° is also sensitive to k_c. However, such reasoning is not correct because equation (3.4) is a mathematical simplification of the more fundamental expression for σ°, namely, equation (3.1). In fact, Miller, et al. (1972) have found that for a Pierson-Moskowitz-Phillips spectral form, a determination of σ° using (3.1) is insensitive to k_c for $k_c \gtrsim 100\ m^{-1}$ while values for σ° obtained from (3.4) show an increased sensitivity.

The primary reason for reviewing the dependence of σ° at normal incidence upon s_m^2 is to point out that this relationship is an approximation which can lead to erroneous conclusions. Therefore, extreme care should be exercised in relating σ°, s_m^2 and spectral cutoff wavenumbers.

Because the theory developed by Huang for current-wave interaction is limited to the gravity wave range only, we note that it is inadequate to permit a determination of the effect of currents on σ° at normal incidence. This observation is a consequence of the fact that we require the complete spectrum in order to compute $\rho_n(r)$ as required in equation (3.1), or, for

that matter, to compute s_m^2 as required in (3.4). As a result of this limitation, we can only very crudely estimate the effect of currents on the normal incidence backscattering cross section. Only after the oceanographic analysis is extended into the capillary range of the spectrum, can we accurately determine the sensitivity of σ° at normal incidence to currents.

To estimate the effect of currents on σ°, we will use the results derived by Huang for s_m^2 in conjunction with equation (3.4). In order to not violate the gravity wave assumptions implicit in Huang's analysis, we will take the cutoff wavenumber to be 20.9 m^{-1} ($\lambda_c = 0.3$ m). As noted above, this value is felt to be somewhat conservative, i.e., actual values will probably be larger. As will be shown below, as k_c increases so does the sensitivity of $\sigma^\circ(U)$ to current changes; thus, the results presented here should be considered to be a lower bound estimate of the sensitivity of σ° to current changes.

From equation (3.4), the ratio of $\sigma^\circ(U)$ to $\sigma^\circ(U=0)$ is given by

$$\frac{\sigma^\circ(U)}{\sigma^\circ(U=0)} = \frac{s_m^2(U=0)}{s_m^2(U)} \tag{3.5}$$

Huang, et al. (1972) have derived the following relationships for $s_m^2(U=0)$ and $s_m^2(U)$;

$$s_m^2(U=0) = B \log(k_c w^2/g) \tag{3.6}$$

and

$$s_m^2(U) = 2B \left\{ \ln\left(\frac{U+w}{U+\sqrt{g/k_c}}\right) + 6(X-Y) - \frac{15}{2}\left(X^2-Y^2\right) \right.$$

$$+ \frac{20}{3}\left(X^3-Y^3\right) - \frac{15}{4}\left(X^4-Y^4\right) + \frac{6}{5}\left(X^5-Y^5\right)$$

$$\left. - \frac{1}{6}\left(X^6-Y^6\right) \right\} \quad , \qquad (3.7)$$

where B is the equilibrium range spectral constant (4.05×10^{-3}) and

$$X = \frac{U}{U+w}$$

$$Y = \frac{U}{U+\sqrt{g/k_c}} \quad .$$

A plot of $\sigma^\circ(U)/\sigma^\circ(U=0)$ is shown in Figure 3.1 as a function of current and wind speed. The same directional convention for U and w as was used for the Bragg scatter computation is used here. We note from Figure 3.1 that the normal incidence case is not as sensitive to current as the Bragg scatter geometry. However, it should be noted that Figure 3.1 represents the most pessimistic estimate of the sensitivity of $\sigma^\circ(U)/\sigma^\circ(U=0)$ for normal incidence to current while the same curve for the Bragg scatter case is optimistic. That is, actual cross-section measurements may show that the sensitivities of $\sigma^\circ(U)/\sigma^\circ(U=0)$, for both normal and wide angles of incidence, to changes in current are more comparable than is indicated in Figures 2.1 and 3.1.

Another point to note in Figure 3.1 is the dependence of $\sigma^\circ(U)/\sigma^\circ(U=0)$ on wind speed. Thus, in order to relate changes in $\sigma^\circ(U)/\sigma^\circ(U=0)$ to the magnitude of current we would require some <u>a priori</u> knowledge about the wind speed so that we know which of the curves we are to use in Figure 3.1. Such a measure of wind speed may be obtainable from the waveform recorded by a short pulse normal incidence radar so this is not a totally defeating objection.

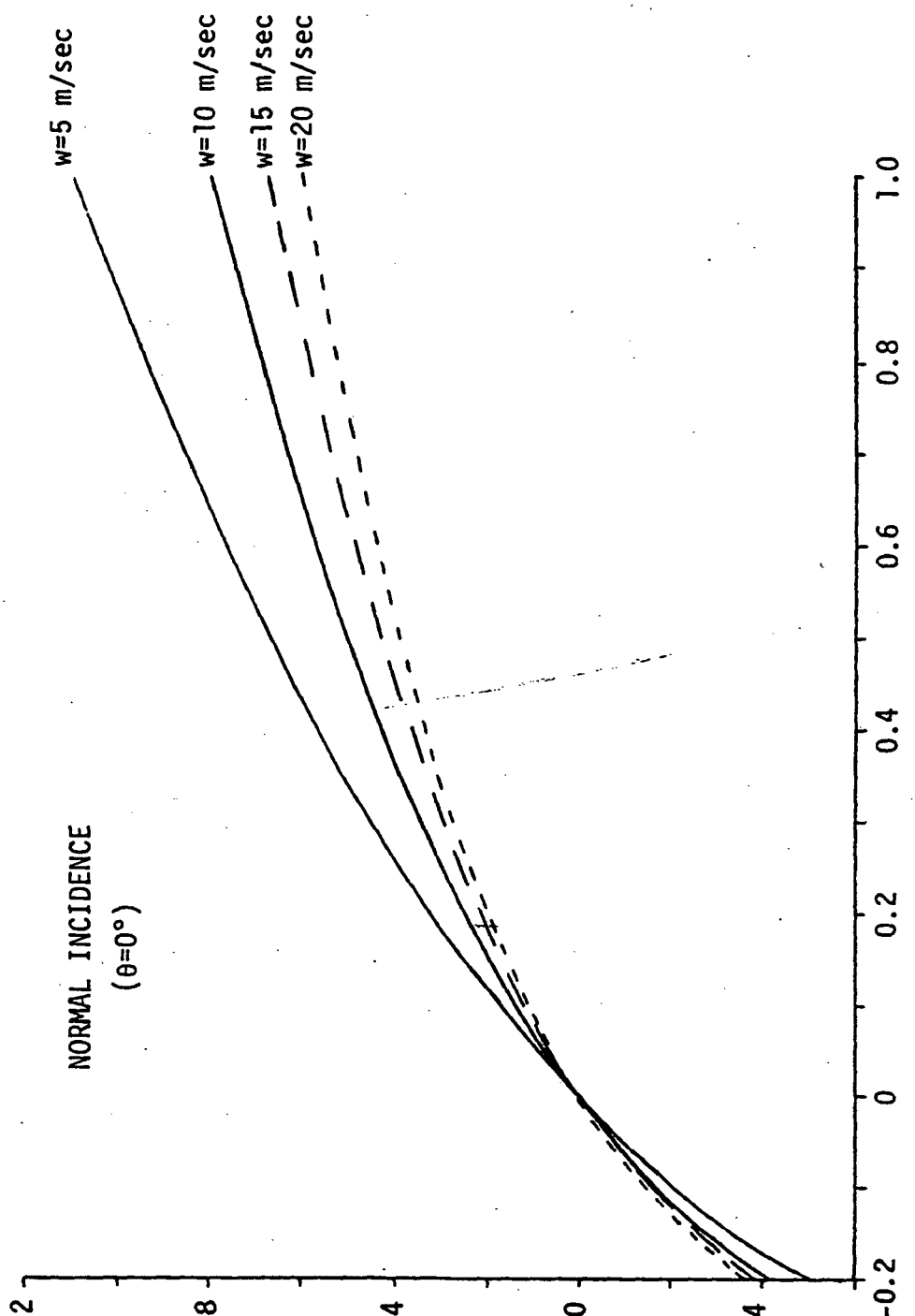

Figure 3.1. Dependence of normal incidence backscattering cross-section upon current.

From a practical standpoint, the near normal incidence measurement would seem to be more feasible in terms of satellite sensors since high gain antennas can be used because the radar frequency may be made very high. In addition, for parallel wind and current, the influence of current will increase the signal-to-noise ratio over the no current condition. Therefore, whereas the Bragg scatter result yields a greater sensitivity, the variance of the measurement may be large due to low signal-to-noise ratio. For normal incidence measurements, the sensitivity may be somewhat smaller but the variance of the measurement will also be small due to the high signal-to-noise ratio. Thus, we conclude that the normal incidence measurement may be as good a sensor of current as the Bragg scatter measurement when practical considerations are properly accounted for.

The results of the analysis presented here definitely justify an experimental program to determine if currents can be detected through cross section measurements. Existing equipment such as the NRL four-frequency radar and the NRL nanosecond radar could provide both wide angle and normal incidence backscattering measurements. It is strongly recommended that such an experimental program be initiated.

REFERENCES

Boone, J. H.

1974. Current-wave interaction patterns near a tidal inlet. M. S. Thesis, North Carolina State University, 97 pp.

Cox, C. S. and W. H. Munk

1954a. Statistics of the sea surface derived from sun glitter, J. Marine Res., 13, 198-227.

Crapper, G. D.

1972. Non-linear gravity waves on steady non-uniform currents. J. Fluid Mech., 52, 713-724.

Huang, N. E., D. T. Chen, C. C. Tung and J. R. Smith

1972. Interactions between steady non-uniform currents and gravity waves with applications for current measurements. J. Phys. Oceanography, 2, 420-431.

Huang, N. E., F. Y. Sorrell, S. R. Long and C. C. Tung

1974. Ocean Dynamic Studies. NASA-CR-137467, 180 pp.

Longuet-Higgins, M. S. and R. W. Stewart

1960. Changes in the form of short gravity waves on long waves and tidal currents. J. Fluid Mech. 8, 565-583.

Longuet-Higgins, M. S. and R. W. Stewart

1964. The changes in amplitude of short gravity waves on steady non-uniform currents. J. Fluid Mech. 10, 529-549.

Longuet-Higgins, M. S. and R. W. Stewart

1964. Radiation stresses in waterwaves; a physical discussion with applications. Deep Sea Research 11, 529-562.

Longuet-Higgins, M. S., D. E. Cartwright and N. D. Smith

1963. Observations of the directional spectrum of sea waves using the motions of a floating buoy. Ocean Wave Spectra, Prentice-Hall, 111-136.

Miller, L. S., G. S. Brown and G. S. Hayne

1972. Analysis of satellite altimeter signal characteristics and investigation of sea-truth data requirements, NASA-CR-137465.

REFERENCES (Cont.)

Miller, L. S. and G. S. Brown

1974. Engineering studies related to the GEOS-C radar altimeter, NASA-CR-137462.

Mitchell, J. H.

1893. The highest waves in water. Journal of Science 36, 5th ser., 430-437.

Parson, C. L.

1974. Some observation of ocean backscatter using SKYLAB S-193 Radar Altimeter data. Trans. A.G.U. 55.

Phillips, O. M.

1966. The dynamics of the upper ocean. Cambridge U. press, 261 pp.

Yaplee, B. S., A. Shapiro, D. L. Hammond, B. D. Au and E. A. Uliana

1971. Nanosecond radar observations of the ocean surface from a stable platform. Geoscience Electronic, GE-9, 170-174.